NRC·CNRC

NRC Publications Archive
Archives des publications du CNRC

Arsenal of nanobodies shows broad-spectrum neutralization against SARS-CoV-2 variants of concern in vitro and in vivo in hamster models

Rossotti, Martin A.; Van Faassen, Henk; Tran, Anh T.; Sheff, Joey; Sandhu, Jagdeep K.; Duque, Diana; Hewitt, Melissa; Wen, Xiaoxue; Bavananthasivam, Jegarubee; Beitari, Saina; Matte, Kevin; Laroche, Geneviève; Giguère, Patrick M.; Gervais, Christian; Stuible, Matthew; Guimond, Julie; Perret, Sylvie; Hussack, Greg; Langlois, Marc-André; Durocher, Yves; Tanha, Jamshid

This publication could be one of several versions: author's original, accepted manuscript or the publisher's version. / La version de cette publication peut être l'une des suivantes : la version prépublication de l'auteur, la version acceptée du manuscrit ou la version de l'éditeur.
For the publisher's version, please access the DOI link below./ Pour consulter la version de l'éditeur, utilisez le lien DOI ci-dessous.

Publisher's version / Version de l'éditeur:
https://doi.org/10.1038/s42003-022-03866-z
Communications Biology, 5, 1, 2022-09-09

NRC Publications Archive Record / Notice des Archives des publications du CNRC :
https://nrc-publications.canada.ca/eng/view/object/?id=ee94cac8-5d64-4ff0-a0dc-aa71012bd948
https://publications-cnrc.canada.ca/fra/voir/objet/?id=ee94cac8-5d64-4ff0-a0dc-aa71012bd948

Access and use of this website and the material on it are subject to the Terms and Conditions set forth at
https://nrc-publications.canada.ca/eng/copyright
READ THESE TERMS AND CONDITIONS CAREFULLY BEFORE USING THIS WEBSITE.

L'accès à ce site Web et l'utilisation de son contenu sont assujettis aux conditions présentées dans le site
https://publications-cnrc.canada.ca/fra/droits
LISEZ CES CONDITIONS ATTENTIVEMENT AVANT D'UTILISER CE SITE WEB.

Questions? Contact the NRC Publications Archive team at PublicationsArchive-ArchivesPublications@nrc-cnrc.gc.ca. If you wish to email the authors directly, please see the first page of the publication for their contact information.

Vous avez des questions? Nous pouvons vous aider. Pour communiquer directement avec un auteur, consultez la première page de la revue dans laquelle son article a été publié afin de trouver ses coordonnées. Si vous n'arrivez pas à les repérer, communiquez avec nous à PublicationsArchive-ArchivesPublications@nrc-cnrc.gc.ca.

National Research Council Canada | Conseil national de recherches Canada

Canada

communications biology

ARTICLE

https://doi.org/10.1038/s42003-022-03866-z OPEN

Arsenal of nanobodies shows broad-spectrum neutralization against SARS-CoV-2 variants of concern in vitro and in vivo in hamster models

Martin A. Rossotti[1], Henk van Faassen[1], Anh T. Tran[1], Joey Sheff[1], Jagdeep K. Sandhu[1,2], Diana Duque[1], Melissa Hewitt[1], Xiaoxue Wen[1], Jegarubee Bavananthasivam[1], Saina Beitari[1], Kevin Matte[2], Geneviève Laroche[2], Patrick M. Giguère[2,3], Christian Gervais[4], Matthew Stuible[4], Julie Guimond[4], Sylvie Perret[4], Greg Hussack[1], Marc-André Langlois[2], Yves Durocher[4,5] & Jamshid Tanha[1,2]✉

Nanobodies offer several potential advantages over mAbs for the control of SARS-CoV-2. Their ability to access cryptic epitopes conserved across SARS-CoV-2 variants of concern (VoCs) and feasibility to engineer modular, multimeric designs, make these antibody fragments ideal candidates for developing broad-spectrum therapeutics against current and continually emerging SARS-CoV-2 VoCs. Here we describe a diverse collection of 37 anti-SARS-CoV-2 spike glycoprotein nanobodies extensively characterized as both monovalent and IgG Fc-fused bivalent modalities. The nanobodies were collectively shown to have high intrinsic affinity; high thermal, thermodynamic and aerosolization stability; broad subunit/domain specificity and cross-reactivity across existing VoCs; wide-ranging epitopic and mechanistic diversity and high and broad in vitro neutralization potencies. A select set of Fc-fused nanobodies showed high neutralization efficacies in hamster models of SARS-CoV-2 infection, reducing viral burden by up to six orders of magnitude to below detectable levels. In vivo protection was demonstrated with anti-RBD and previously unreported anti-NTD and anti-S2 nanobodies. This collection of nanobodies provides a potential therapeutic toolbox from which various cocktails or multi-paratopic formats could be built to combat multiple SARS-CoV-2 variants.

[1] Human Health Therapeutics Research Centre, Life Sciences Division, National Research Council Canada, Ottawa, ON, Canada. [2] Department of Biochemistry, Microbiology and Immunology, Faculty of Medicine, University of Ottawa, Ottawa, ON, Canada. [3] University of Ottawa Brain and Mind Research Institute, University of Ottawa, Ottawa, ON, Canada. [4] Human Health Therapeutics Research Centre, Life Sciences Division, National Research Council Canada, Montréal, QC, Canada. [5] Département de biochimie et médecine moléculaire, Université de Montréal, Montréal, QC, Canada. ✉email: Jamshid.Tanha@nrc-cnrc.gc.ca

Declared a pandemic in March 2020 by the World Health Organization (covid19.who.int), coronavirus disease 2019 (COVID-19), caused by severe acute respiratory syndrome coronavirus 2 (SARS-CoV-2), remains a significant global health and economic burden. As of 20 August 2022, over 595 million individuals have been infected world-wide, of which over 6.4 million have died (coronavirus.jhu.edu). The toll on public health has been exacerbated with the continual emergence of SARS-CoV-2 variants of concern (VoCs)[1,2]. These VoCs, which include Alpha (B.1.1.7), Beta (B.1.351), Gamma (P.1), Delta (B.1.617.2), and Omicron (B.1.1.529), can evade COVID-19 vaccines and therapeutics to different extents, and the evolutionary trajectory of the virus variants predicts newer VoC escape mutants to emerge in the future[1–9].

Key to SARS-CoV-2 infection is its surface-displayed spike glycoprotein (S)[10–14], a homotrimeric protein where each protomer ectodomain format consists of S1 and S2 subunits. S1 is further delineated by an N-terminal domain (NTD), a receptor-binding domain (RBD) and subdomains SD1 and SD2. The spike glycoprotein mediates cell entry, a critical first phase in the infection process, through two discrete but concerted steps. In the first, virus-cell binding step, the RBD, essentially through its receptor-binding motif (RBM), binds to its host receptor angiotensin-converting enzyme II (ACE2). This is followed by the second, virus-cell fusion step, which is mediated by the S2 subunit and concludes the viral cell entry event. Spike glycoprotein is the primary target for COVID-19 therapeutic antibodies, which operate by stopping virus cell entry *via* blocking the cell binding and/or fusion step. In particular, the mechanism of action of most potent neutralizing antibodies involves binding to the RBD, although neutralizing antibodies targeting the NTD domain[15–20] and the S2 subunit[21,22] have also been reported.

Although many COVID-19 immunotherapies are based on monoclonal antibodies (mAbs), single-domain antibodies (mostly V_HHs) are also being pursued as alternative therapeutics[4,23–48]. V_HHs (nanobodies) are the variable domains of camelid heavy-chain antibodies responsible for antigen recognition. One nanobody (VHH-72/XVR011) has already entered clinical trials for COVID-19 therapy[30,39,49]. V_HHs offer potential advantages over mAbs as COVID-19 immunotherapeutics, most notably because of their stability against aerosolization that allows for convenient, low-cost, and effective needle-free delivery of V_HHs into the key site of infection (lungs) by inhalation[40,41,50–52]. Importantly, V_HHs permit modular assembly of multimeric/multi-paratopic nanobody constructs with drastically improved efficacy and cross-reactivity/neutralization breadth across VoCs[35,37]. Multispecific V_HH constructs can also be designed to target confined geometric spaces on the surface of the target antigen without nanobody clash, a feature not achievable with larger mAbs. Critically, with small size and frequently extended CDR3s, V_HHs can reach cryptic epitopes that are hidden from mAbs and conserved across SARS-CoV-2 VoCs, allowing for the development of broad-spectrum nanobody therapeutics against current and future VoCs[35,39,40].

Here we report the isolation and extensive characterization of a large collection of SARS-CoV-2-targeting nanobodies. Monovalent V_HH and bivalent V_HH-Fc formats were assessed for binding affinity; thermal, thermodynamic and aerosol stability; epitopic diversity; S subunit/domain specificity; cross-reactivity to multiple betacoronavirus subgenera and VoCs; in vitro cross-neutralization potencies against all existing VoCs; and in vivo neutralization efficacies using a hamster model of infection. Multiple neutralization mechanisms of action are possible through V_HH binding to RBD, NTD, and S2, including inhibiting the virus-cell binding and/or fusion steps. This robust collection of nanobodies provides a foundation for development of effective broad-spectrum therapeutics (monotherapy, cocktails, or multimerics/multi-paratopics) that could combat several SARS-CoV-2 variants.

Results

Llama immunization and serum analyses. Prior to immunization, serology and panning experiments, purified SARS-CoV-2 spike glycoprotein (S) antigens were validated for functionality in adsorbed/captured states on microtiter wells (Supplementary Fig. 1 and Supplementary Table 1). Two llamas (Green & Red) were immunized with SARS-CoV-2 Wuhan-Hu-1 (Wuhan) S fragments. Specifically, Green was primed with S and boosted with three doses of RBD fragment, while Red received four doses of S. Both llamas produced a strong and specific immune response to S, S1, S2, and RBD with Green consistently outperforming Red (up to 10-fold) across all four target proteins (Supplementary Fig. 2a). That Green outperformed Red in terms of response to S2 despite the fact that it was immunized once with "S2" (*i.e.*, S) as opposed to four times for Red is notable. However, outbred animals, such as the llamas in the current study, are notorious for generating heterogenous immune responses even when they are immunized with the same antigen. Analyses of total polyclonal sera by flow cytometry-based surrogate neutralization assays (SVNA) showed a more potent neutralizing antibody response generated by Green (Supplementary Fig. 2b).

Phage display library construction, selection, and screening. Two phage display libraries, Green and Red, were constructed using day 28 peripheral blood mononuclear cells (PBMCs) and separately subjected to two rounds of panning against S fragments. To further maximize for V_HH diversity, panning was performed under multiple selection conditions (P1–P6; see Methods section) to direct selection towards S-, S1-, S2-, RBD-, NTD-, and RBM-specific binders. Monoclonal phage ELISA combined with DNA sequencing performed across all screens identified 37 unique V_HHs (Fig. 1a and Supplementary Fig. 3a) that demonstrated diverse CDR3 lengths (Supplementary Fig. 3b). Most V_HHs originated from llama Green, 26 vs 11 from llama Red (Fig. 1a). Llama Green, which was predominantly immunized with RBD, yielded a higher proportion of RBD-specific V_HHs (15 RBD, six NTD, five S2) compared to llama Red which was immunized with only S and yielded mostly S2-specific V_HHs (two RBD, three NTD, six S2).

Selected V_HHs were then (i) cloned as fusions to the biotinylation acceptor peptide (BAP) and His_6 tags and produced in *E. coli*; and (ii) cloned in fusion with human IgG1 hinge-Fc domain (V_HH-Fc) and produced in HEK293-6E cells.

Binding characteristics of V_HHs and V_HH-Fcs. V_HHs/V_HH-Fcs were tested by SPR and ELISA against recombinant Wuhan SARS-CoV-2 S, S1, RBD, NTD and S2 proteins to determine affinities and subunit/domain specificities (Fig. 1b; Supplementary Fig. 4; and Supplementary Tables 2–3). V_HHs bound with high affinity, with the majority of K_Ds in the single-digit-nM to pM range. Three clusters of V_HHs were identified: 17 RBD-specific V_HHs, nine NTD-specific V_HHs (no reactivity to RBD, bound S and S1) and 11 S2-specific V_HHs (Fig. 1b). The domain specificity of the NTD binders was confirmed in subsequent ELISAs (Supplementary Fig. 4b and Supplementary Table 3). By flow cytometry, V_HH-Fcs bound SARS-CoV-2 S (Wuhan) in a more natural context on the cell membrane of CHO cells ($CHO^{55E1™}$) stably transfected with the S protein (Fig. 1c; Supplementary Fig. 5; and Table 1). High apparent affinities (EC_{50}apps) in the single-digit-nM to pM range were observed for the majority of V_HH-Fcs.

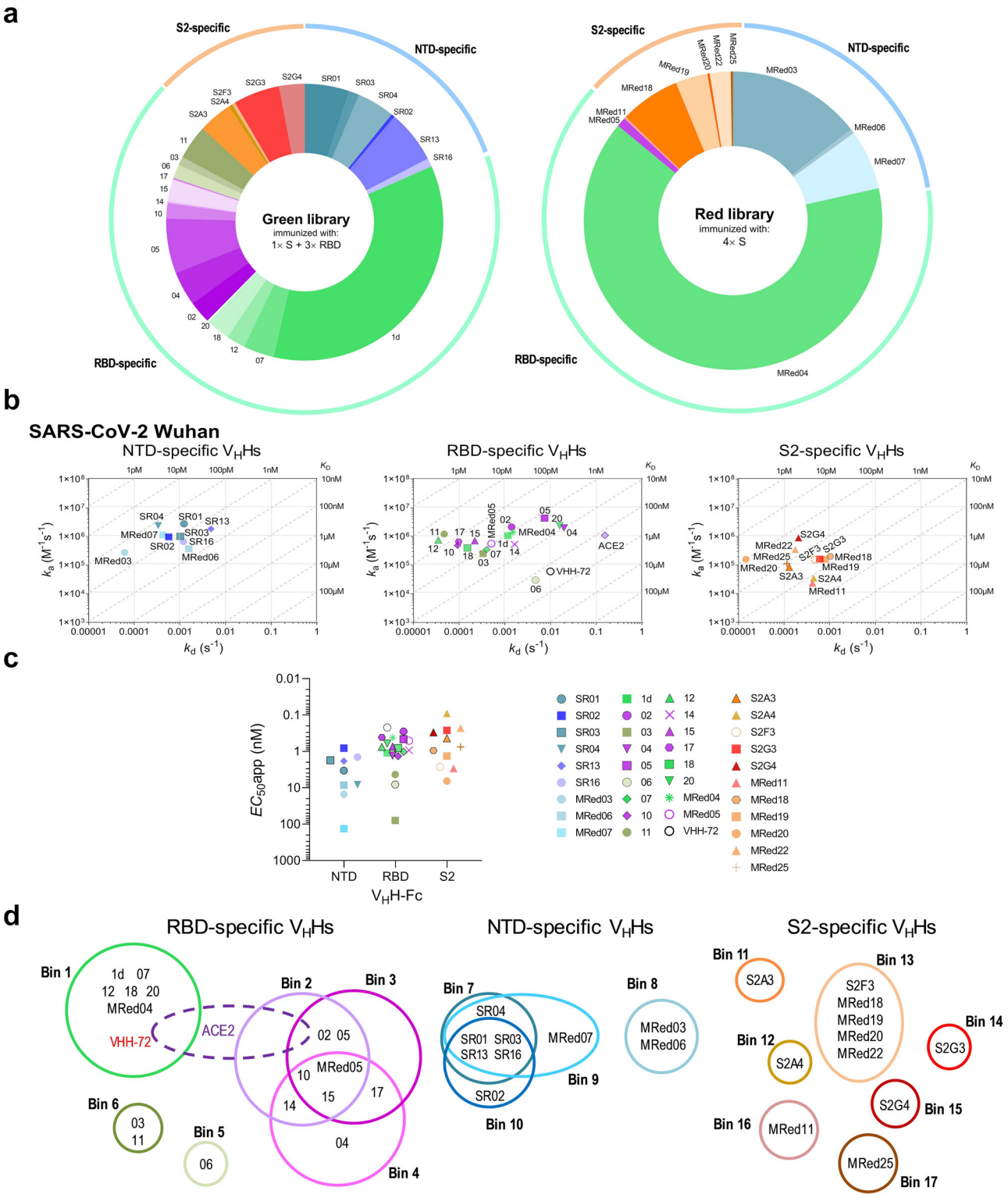

To identify the number of non-overlapping epitopes, V_HHs were subjected to epitope binning experiments by SPR and sandwich ELISA. SPR assays were performed by injecting paired combinations of eight RBD-specific V_HHs, all NTD-specific and all S2-specific V_HHs over a SARS-CoV-2 spike glycoprotein surface (Supplementary Fig. 6a). A conceptually similar assay to SPR was performed by sandwich ELISA to assess the remaining nine RBD-specific V_HHs (Supplementary Fig. 6b). From the 37 V_HHs tested, 17 epitope bins were identified: 6 for RBD-specific V_HHs, 4 for NTD-specific V_HHs, and 7 for S2-specific V_HHs (Fig. 1d and Table 1). The benchmark VHH-72 binned with RBD-specific V_HHs 1d, 07, 12, 18, 20 and MRed04. With the exception of V_HH 04, all remaining bin 1, 2, 3, and 4 V_HHs (13 in total), as well as VHH-72, binned with ACE2, consistent with them being potent neutralizers (see below).

V_HHs were examined for cross-reactivity to a collection of spike glycoprotein fragments from various coronavirus genera and SARS-CoV-2 variants by ELISA and SPR. In ELISA (Fig. 2a and Table 1), many V_HH-Fcs cross-reacted with the S protein from VoCs Alpha, Beta, Gamma, Delta, Omicron (B.1.1.529), and

Fig. 1 Selection, binding affinity, subunit/domain specificity and epitope binning of anti-SARS-CoV-2 S V_HHs. a Library origin, relative proportion and subunit/domain specificity of the 37 anti-SARS-CoV-2 S V_HHs selected from the Green and Red libraries by employing six panning strategies P1–P6 (*see* also Supplementary Fig. 3). Green library V_HHs were isolated from the llama immunized once with S and three times with RBD. Red library V_HHs were isolated from the llama immunized four times with S. Source data used to generate the figure are included in Supplementary Data 1. **b** On-/off-rate maps summarizing V_HH kinetic rate constants, k_as and k_ds, determined by SPR. Diagonal lines represent equilibrium dissociation constants, K_Ds (*see* also Table 1). Maps were constructed using the V_HH binding data (Supplementary Fig. 4; Supplementary Table 2) against SARS-CoV-2 Wuhan S (all except 12 and MRed05) or RBD (12 and MRed05). V_HH subunit/domain specificities were determined by SPR and ELISA (Supplementary Fig. 4; Supplementary Tables 2–3). Anti-SARS-CoV S VHH-72 which cross-reacts with SARS-CoV-2 RBD[30] and monomeric ACE2 (ACE2-H_6) were included as benchmark/reference binders. **c** Binding of SARS-CoV-2 S V_HH-Fcs to S-expressing CHO cells (CHO-SPK) obtained by flow cytometry. Apparent EC_{50}s (EC_{50}apps) were obtained from graphs in Supplementary Fig. 5 and are included in Table 1. **d** Summary of epitope bins identified by SPR and ELISA (*see* Supplementary Fig. 6). V_HHs are grouped according to their specificity for NTD, RBD or S2 and color-coded based on their epitope bin designation.

Kappa (B.1.617.1; Variant Being Monitored). The exceptions were: (1) RBD-specific V_HHs 1d, 07, 18 and MRed05 did not cross-react with Omicron, 02/05 did not cross-react with Beta, Gamma and Omicron and 04/14/15 did not cross-react with Kappa and 2) S2-specific V_HHs MRed18/MRed19 and MRed22 did not cross-react with Kappa and Omicron, respectively. All nine NTD-specific V_HHs cross-reacted with all variants tested. Additionally, many V_HHs cross-reacted with pangolin CoV, with fewer cross-reacting to SARS-CoV, SARS-like CoV WIV1, bat SARS-like CoV, and civet SARS CoV. These viruses, including variants, are all of the Betacoronavirus Sarbecovirus subgenus. None of the antibodies tested cross-reacted with the remaining 11 non-Sarbecovirus Betacoronavirus, Alphacoronavirus, Deltacoronavirus or Gammacoronavirus. The broadly cross-reactive antibodies included V_HHs targeting all three regions of the S protein (RBD, NTD, S2). The most broadly cross-reactive V_HHs recognizing 11–12 viruses, including SARS-CoV-2 variants, were two NTD binders (SR01, SR02), six RBD binders (1d, 07, 11, 12, 20, MRed04) and six S2 binders (S2F3, S2G3, S2G4, MRed18, MRed19, MRed20). The VHH-72 benchmark was also broadly cross-reactive, although it did not cross-react with Omicron. The panel of V_HHs had similar cross-reactivity profiles to human ACE2, except that ACE2 did not bind civet SARS-CoV S and, unsurprisingly, bound HCoV-NL63 S (Fig. 2a)[53,54].

All 37 V_HHs were tested for cross-reactivity against SARS-CoV by both ELISA and SPR, of which 14 were positive by ELISA. By SPR, 12 out of these 14 ELISA-positive V_HHs cross-reacted with SARS-CoV S, most with comparably high affinities (Fig. 2b; Table 1; Supplementary Fig. 7a; and Supplementary Table 4). Seven of these V_HHs were S2-specific, four RBD-specific and one NTD-specific. Against the Alpha and Beta variants, the SPR cross-reactivity data, performed with all 37 V_HHs, were consistent with ELISA, except for V_HHs 04 and 14 which were negative or very weak for binding to the Beta variant by SPR. All 37 V_HHs bound the Alpha variant S protein, 34 of which were also cross-reactive to the Beta variant S protein (Fig. 2c; Supplementary Fig. 7b; Table 1; and Supplementary Table 4). Thirteen out of 17 RBD-specific V_HHs bound all three variants with similar affinities, except for V_HHs 10, 15, and 17 which bound to the Beta variant with 40–50-fold weaker affinity; the remaining four that did not bind the Beta variant showed cross-reactivity with the Alpha variant with similar (04, 14) or reduced (~5-fold [05] and ~20-fold [02]) affinity relative to the Wuhan variant. All NTD-specific and S2-specific V_HHs cross-reacted with the three variants with essentially the same or similar affinities. The loss of binding for some of the ELISA-positive nanobodies in SPR assays could be due to the loss of binding avidity (V_HH-Fc was used in ELISA vs V_HH in SPR) and/or epitope hindrance on the sensorchip.

Stability characteristics of V_HHs. By size exclusion chromatography (SEC), all 37 V_HHs were shown to lack aggregation (Fig. 3a and Supplementary Fig. 8). V_HHs were highly thermostable[55]: with the exception of four V_HHs which had T_ms of ~60 °C, the remaining 33 V_HHs had T_ms of ~63–80 °C (median: 70.4 °C) (Fig. 3b; Supplementary Fig. 9; and Supplementary Table 5). Conformational stability of a sample set of V_HHs was determined by measuring free energy of unfolding (ΔG^0) in GdnHCl equilibrium denaturation experiments, with ΔG^0 ranging from 21.4 to 53.4 kJ/mol (median: 30.7 kJ/mol), and an m value range of 10.3–19.8 kJ/M*mol (median: 14.6 kJ/M*mol) observed (Fig. 3c; Supplementary Fig. 10; and Supplementary Table 5)[55–59].

Since we planned to test V_HH-Fcs in hamsters for in vivo efficacy, we pre-emptively assessed their in vivo stability and persistence. We chose 1d V_HH-Fc as a representative and included VHH-72 V_HH-Fc, whose modified/enhanced version is currently in a phase 1 clinical trial, as a point of reference. Hamsters were injected intraperitoneally (IP) with 1 mg of each antibody and serum antibody concentration was monitored for up to four days by ELISA. Unsurprisingly, antibody concentration decreases were observed with time (days post-injection). Nonetheless, considerable amounts of 1d V_HH-Fc similar in magnitude to those for VHH-72 benchmark were present in the hamster sera on days 1 and 4 post injection (Fig. 3d), indicating V_HH-Fcs, as with VHH-72, would have the required serum stability and persistence in vivo for the duration of the animal studies.

V_HHs were also examined for their aggregation resistance and stability upon aerosolization. For a few V_HHs, aerosolization induced soluble aggregate formation as determined by SEC, while for others it led to the formation of visible aggregates (Supplementary Fig. 11 and Supplementary Table 6). This resulted in reduced percentage recoveries, measures of V_HH stability against aerosolization, and corresponding to the proportion of V_HHs that remained as soluble monomer following aerosolization (Fig. 3e; Supplementary Fig. 11; and Supplementary Table 6). The majority of V_HHs (18 out of 28 V_HHs tested), however, were stable against aerosolization with high percentage recoveries (Fig. 3e). In addition, several V_HHs still showed a high percentage recovery upon aerosolization (50–70%) despite the formation of some visible aggregates. Comparison of ELISA-derived EC_{50}s of select pre-aerosolized vs post-aerosolized V_HHs clearly demonstrated aerosolization did not compromise the binding activities of V_HHs (Fig. 3e and Supplementary Fig. 11).

Screening for neutralizing V_HHs by surrogate virus neutralization assays. A preliminary screen of a sample of RBD-, NTD-, and S2-specific V_HHs by ELISA- and SPR-based SVNAs identified at least 15 potential neutralizers, predominantly from the RBD-binding cohort (Supplementary Fig. 12 and Supplementary Table 7). A more relevant SVNA, which assessed the ability of antibodies to block binding of S to Vero E6 cells displaying ACE2, was then used as a screen to identify neutralizing V_HHs and V_HH-Fcs. Neutralizing V_HHs displayed similar potencies (IC_{50}: 5–21 nM) and outperformed the benchmark

Table 1 Binding characteristics of SARS-CoV-2 V_HHs.

V_HH/ACE2	Epitope		SARS-CoV-2 Wuhan S	SARS-CoV-2 Alpha S		SARS-CoV-2 Beta S		SARS-CoV S		SARS-CoV-2 S expressing cells[h]
	Bin	Type	SPR (K_D, nM)	ELISA[f]	SPR (K_D, nM)	ELISA[f]	SPR (K_D, nM)	ELISA[f]	SPR (K_D, nM)	FC (EC_{50}app nM)
RBD-specific V_HH										
1d	1	Conf.[d]	0.75	+	0.91	+	1.2	+	–	1.1
02	2/3	Conf.[d]	0.62	+	13.6	–	–	–	–	0.3
03	6	Conf.[d]	1.56	+	1.49	+	4.08	–	–	79
04	4	Conf.[d]	10.2	+	11.7	+	–	–	–	1.3
05	2/3	Conf.[d]	2.6	+	11.4	–	–	–	–	0.5
06	5	Linr.[e]	223	+	229	+	248	–	–	8.1
07	1	Conf.[d]	0.94	+	1.1	+	1.1	+	12.2	1
10	2/3/4	Conf.[d]	0.2	+	0.21	+	9.73	–	–	1.3
11	6	Conf.[d]	0.018	+	0.017	+	0.023	+	0.014	4.3
12[a]	1	Conf.[d]	0.047	+	0.046	+	0.04	+	2.69	0.8
14	2/4	Conf.[d]	2.6	+	2.44	+	wb	–	–	0.9
15	2/3/4	Conf.[d]	0.32	+	0.31	+	22.2	–	–	0.7
17	3/4	Conf.[d]	0.15	+	0.13	+	5.1	–	–	0.4
18	1	Linr.[e]	0.32	+	0.35	+	0.37	–	–	0.8
20	1	Conf.[d]	4.39	+	4.97	+	5.47	+	–	0.6
MRed04	1	Conf.[d]	0.86	+	0.91	+	1.07	+	300	0.4
MRed05[a]	2/3/4	Conf.[d]	0.91	+	0.31	+	0.89	–	–	0.5
VHH-72[b]	1	Conf.[d]	86.2	+	96	+	124	+	6.52	0.2
ACE2[c]	na	na	153	+	18.3	+	131	+	351	1.2
NTD-specific V_HH										
SR01	7/9/10	Linr.[e]	0.56	+	0.59	+	0.2	+	0.154	3.4
SR02	10	Conf.[d]	0.14	+	0.06	+	0.15	+	–	0.8
SR03	7/9/10	Conf.[d]	1.69	+	1.72	+	2.49	–	–	1.7
SR04	7/9	Linr.[e]	0.14	+	0.27	+	0.32	–	–	8.2
SR13	7/9/10	Conf.[d]	3.6	+	5.8	+	7	–	–	1.8
SR16	7/9/10	Conf.[d]	2	+	1.6	+	2.6	–	–	1.4
MRed03	8	Conf.[d]	0.51	+	0.36	+	0.67	–	–	15
MRed06	8	Conf.[d]	5.2	+	5.72	+	7.24	–	–	8.5
MRed07	9	Conf.[d]	0.11	+	0.26	+	0.23	–	–	132
S2-specific V_HH										
S2A3	11	Linr.[e]	0.56	+	2.18	+	0.85	–	–	0.4
S2A4	12	Linr.[e]	12.8	+	9.5	+	15.3	–	–	0.1
S2F3	13	Linr.[e]	3.03	+	+[g]	+	+[g]	+	4.9	2.7
S2G3	14	Linr.[e]	1.87	+	1.78	+	1.85	+	4.27	0.3
S2G4	15	Linr.[e]	0.23	+	0.19	+	+[g]	+	0.8	0.3
MRed11	16	Linr.[e]	6.2	+	13.7	+	6.2	–	–	2.9
MRed18	13	Linr.[e]	6.03	+	12.9	+	6.48	+	22.5	0.9
MRed19	13	Linr.[e]	9.07	+	20.2	+	8.07	+	24.6	1.3
MRed20	13	Linr.[e]	0.092	+	0.55	+	0.45	+	10.7	4.7
MRed22	13	Conf.[d]	0.51	+	0.25	+	+[g]	–	–	0.3
MRed25	17	Conf.[d]	1.02	+	0.28	+	1.6	+	2.29	0.8

na not applicable, *wb* weak binding.
[a]K_Ds were determined by flowing monomeric V_HHs over sensorchip surfaces immobilized with S, except for V_HH 12 and MRed05, which were determined by flowing monomeric RBDs over V_HH-Fc-captured surfaces (Supplementary Table 4).
[b]VHH-72 benchmark is a SARS-CoV S-specific V_HH that cross-reacts with SARS-CoV-2 S[30].
[c]His_6-tagged monomeric ACE2 (ACE2-H_6) was used for SPR assays, human Ig Fc-fused dimeric ACE2 (ACE2-Fc) for ELISA, and cell binding assays by flow cytometry.
[d]Conf., conformational epitope.
[e]Linr., linear epitope.
[f]ELISA was performed at 125 nM (1 μg/mL) V_HH-Fc concentration (Fig. 2a).
[g]+, V_HH bound, but poor fitting precluded K_D determination.
[h]Cell binding was performed by flow cytometry (FC) using V_HH-Fcs.

VHH-72 (IC_{50}: 59 nM) by as much as 12-fold (Supplementary Fig. 13 and Table 2). Compared to V_HHs, a larger number of V_HH-Fcs demonstrated neutralization capabilities (Fig. 4a; Supplementary Fig. 14; and Table 2). While neutralizing monovalent V_HHs did not benefit from reformatting to bivalent V_HH-Fcs (except for the VHH-72 benchmark), several non-neutralizing monovalent V_HHs (three RBD-specific and three NTD-specific) benefitted profoundly from reformatting and were transformed into neutralizers that had potencies similar to other RBD-specific V_HH-Fcs. All S2-specific V_HHs remained non-neutralizing as V_HH-Fcs.

Extending our SVNAs to variants Alpha, Beta, Gamma, Delta, Kappa, and Omicron using all of the RBD-specific and a subset of NTD-specific V_HH-Fcs (Fig. 4b and Supplementary Table 8), several observations were made. First, for cross-neutralizing V_HHs the IC_{50}s across variants did not change considerably. Second, while all Wuhan neutralizers also remained Alpha neutralizers, some lost their capability to inhibit Beta, Gamma, Delta, Kappa, and Omicron with variable cross-neutralizing patterns. In particular, with respect to the RBD-specific V_HHs, the cross-neutralization profiles for Beta vs Gamma and Delta vs Kappa were identical, similarly reflective of the key escape

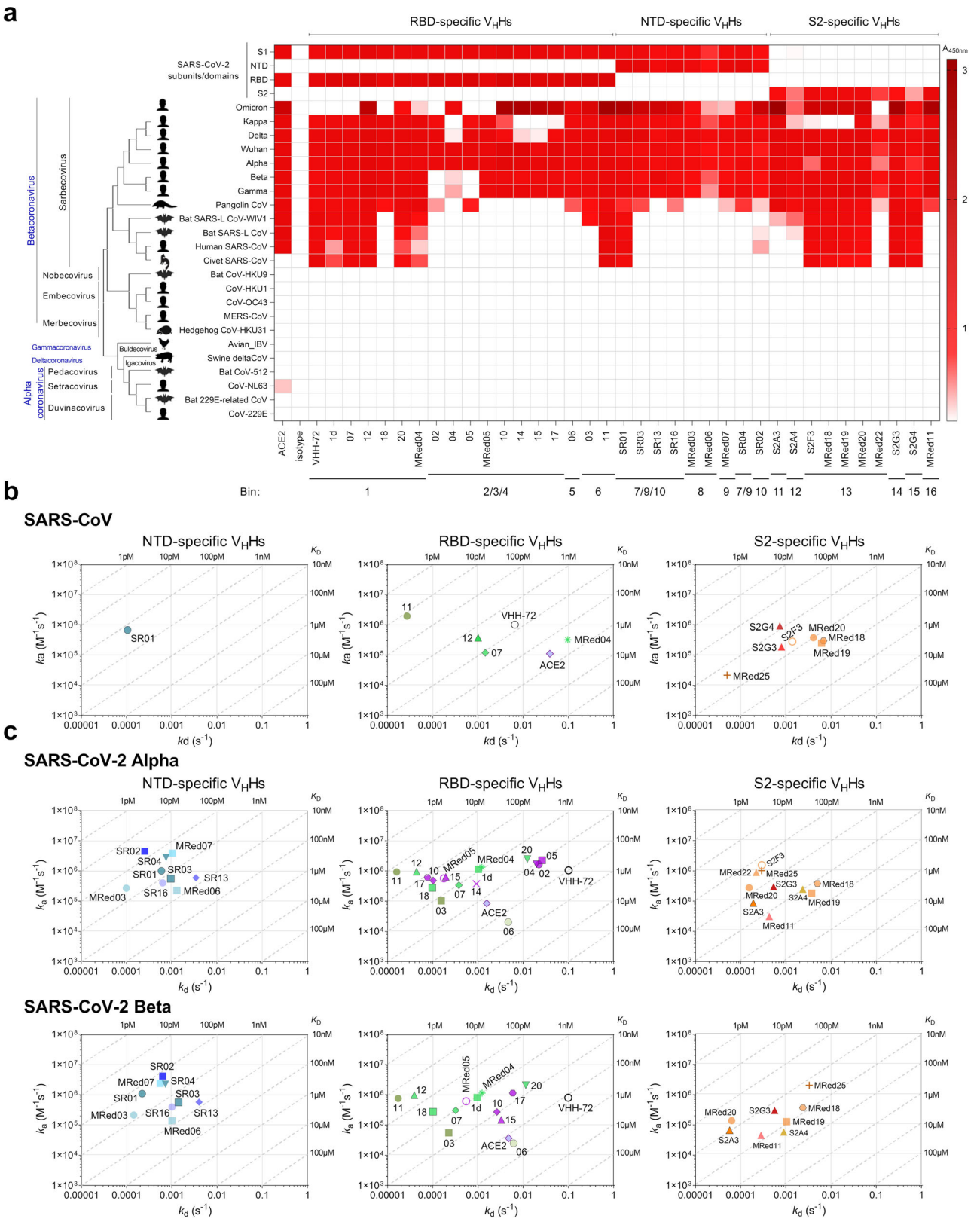

mutations in these variants (K417N, E484K, and N501Y for Beta vs K417T, E484K, and N501Y for Gamma; L452R and T478K for Delta vs L452R and E484Q for Kappa). Third, and importantly, nine out of 20 V_HH-Fcs (eight RBD-specific, one NTD-specific) were Omicron neutralizers, four of which (three RBD-specific, one NTD-specific) neutralized across all variants and SARS-CoV. Of note, VHH-72 neutralized all variants with the exception of Omicron.

Screening for neutralizing V_HHs by pseudotyped and live virus neutralization assays. Using a spike-pseudotyped lentivirus neutralization assay (PVNA), 15 out of the 17 RBD-specific V_HHs

Fig. 2 Cross-reactivity of anti-SARS-CoV-2 S V_HHs. Data are organized based on V_HH subunit/domain specificity and epitope bin designation (*see* Fig. 1d). **a** ELISA showing the cross-reactivity of V_HHs against various coronavirus spike glycoprotein fragments, S, S1, S2, RBD and NTD. Shades of red represent binding, colorless boxes represent no binding. Assays were performed at a single V_HH-Fc concentration. The "isotype" control (A20.1 V_HH-Fc) shows no binding to S. Anti-SARS-CoV VHH-72 and ACE2-Fc were included as references. The phylogenetic tree of spike glycoproteins was constructed using MEGA11[98]. Source data used to generate the figure are included in Supplementary Data 1. **b, c** On-/off-rate maps summarizing V_HH kinetic rate constants, k_as and k_ds determined by SPR for the binding of V_HHs to SARS-CoV S (**b**) and SARS-CoV-2 Alpha and Beta S (**c**). Diagonal lines represent equilibrium dissociation constants, K_Ds (*see* also Table 1). S2F3 cross-reacted to Alpha and Beta, as did S2G4 and MRed22 to Beta; however, poor fitting of SPR data precluded determining their k_as, k_ds and K_Ds, hence their exclusion from relevant graphs. Maps were constructed using the V_HH binding data from Supplementary Fig. 7 and Supplementary Table 4. Anti-SARS-CoV S VHH-72 and the monomeric ACE2 (ACE2-H_6) are included as benchmark/reference binders.

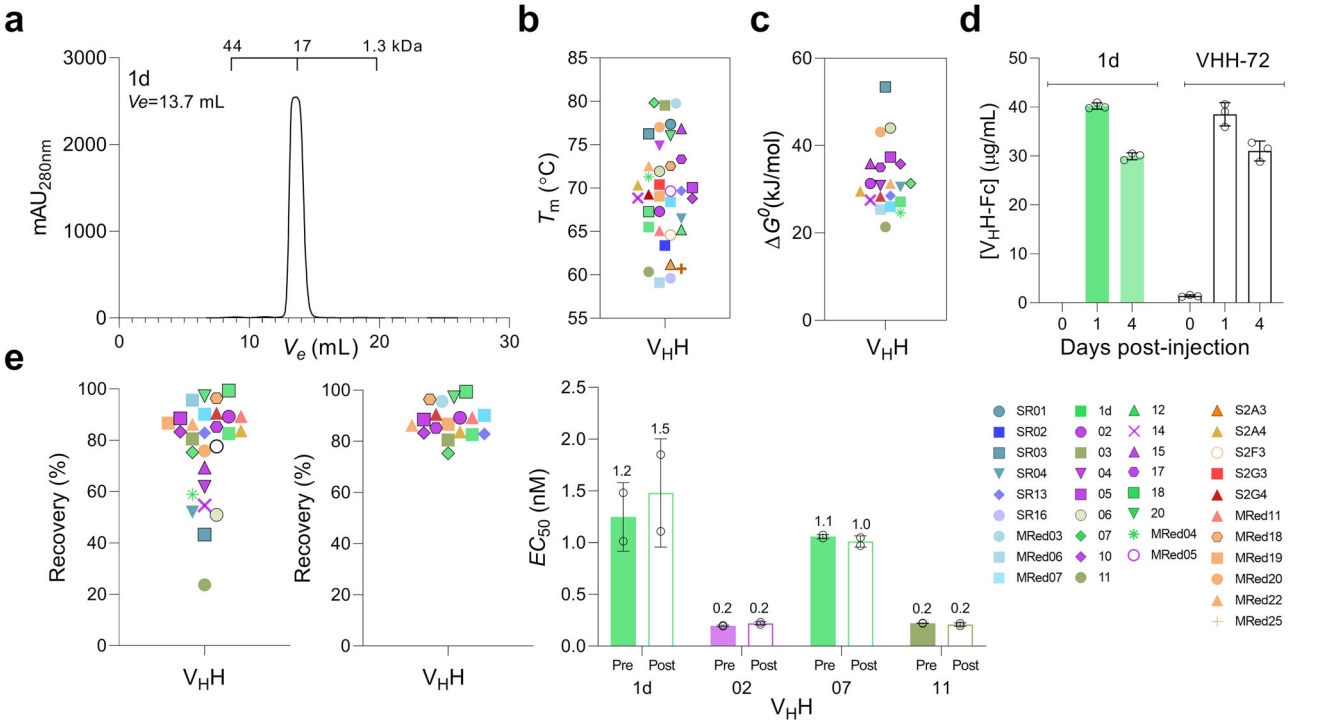

Fig. 3 Stability of anti-SARS-CoV-2 S V_HHs. a Representative SEC profile demonstrating the aggregation resistance of V_HHs. The elution volume (V_e) positions of molecular mass standards (44 kDa, 17 kDa, 1.3 kDa) are marked. See Supplementary Fig. 8 for the full dataset. **b** Summary of V_HH T_m data. T_ms were obtained from plots of % folded vs temperature (Supplementary Fig. 9; Supplementary Table 5). **c** Summary of V_HH ΔG^0 data. ΔG^0 (as well as other thermodynamic parameters, C_m and m values) are reported in Supplementary Table 5. **d** In vivo stability and persistence of V_HHs. Stability and persistence were determined by monitoring the concentration of a representative V_HH-Fc (1d) in hamster blood at various days post-injection by ELISA. VHH-72-Fc was used as the benchmark. Error bars indicate standard deviation (SD) of three biological replicates (animals). **e** Stability of V_HHs against aerosolization. Summary of % recovery of all (left panel) and lead (middle panel) V_HHs are shown. Percent recovery represents the proportion of a V_HH that remained soluble monomer following aerosolization. Graphs were generated based on the data in Supplementary Fig. 11a and Supplementary Table 6. Open circle in **e** (Left panel) represents benchmark VHH-72. **e** (right panel) Activity of pre- vs post-aerosolized V_HHs expressed in terms of antigen binding (EC_{50}). EC_{50}s were determined by ELISA. Error bars indicate standard deviation (SD) of two technical replicates. V_HHs in **b**, **c**, **e** (left panel) and **e** (middle panel) are color-coded based on their epitope bin designation (*see* Fig. 1d). Source data used to generate Fig. 3a, d and e (right panel) are included in Supplementary Data 1.

tested were found to be neutralizing, and with the exception of 03 (IC_{50}: 0.91 μM) and 06 (IC_{50}: 2.5 μM), the V_HHs were potent neutralizers (IC_{50} range: 39–196 nM; median: 48 nM) (Supplementary Fig. 15a and Table 2). (Lack of sufficient quantities of RBD V_HHs 12 and MRed05 precluded them from further assessment by PVNA.) For NTD-specific V_HHs, three of nine were neutralizing: two with similar IC_{50}s of 188 nM (SR01) and 269 nM (SR03) and one with an IC_{50} of 41 nM (SR13), comparable to the most potent RBD-specific V_HHs. Reformatting to V_HH-Fc had a universal enhancing effect on neutralization potencies of V_HHs irrespective of epitope bin origin (Fig. 4a; Supplementary Fig. 15b; and Table 2). For RBD-specific V_HHs, potency increases (IC_{50} decreases) of 2–100-fold were observed; only one V_HH (18) was unaffected with reformatting (IC_{50} range: 2.3–30.8 nM; median: 7.6 nM). NTD-specific V_HH-Fcs demonstrated weaker potencies (IC_{50} range: 11.3–86.9 nM; median: 18.5 nM; four of nine non-neutralizing). However, bivalency also substantially improved (~9-fold) the potencies of SR01 and SR03 and transformed a non-neutralizing V_HH (SR16) into a potent neutralizing V_HH-Fc. Consistent with the aforementioned SVNA results and previous data[30], the VHH-72 benchmark also improved, elevated from a weak V_HH (IC_{50}: 490 nM) to a strong V_HH-Fc (25 nM) neutralizer. S2-specifiic V_HHs remained non-neutralizing with reformatting.

All 22 RBD- and NTD-specific V_HH-Fcs that were neutralizing by PVNA were also neutralizing in a live virus neutralization

Table 2 Neutralization potencies of V_HHs against SARS-CoV-2 Wuhan and variants.

V_HH	Epitope bin	SVNA IC_{50} (nM)[c]		PVNA IC_{50} (nM)[c]		LVNA IC_{50} (nM)[c]			
		V_HH	V_HH-Fc	V_HH	V_HH-Fc	V_HH-Fc			
						Wuhan	Alpha	Beta	Omicron
RBD-specific V_HH									
1d	1	8.6	5.4	50	16.7	1.94	0.37	2.14	nd[e]
02	2/3	5.1	5	43	6.5	0.12	0.09	-	nd[e]
03	6	-	-	910	26.6	58	16	62	~150
04	4	-	11.7	111	26.6	1.65	2.3	-	6.03
05	2/3	9.5	6.7	79	2.3	0.0008	0.03	-	nd[e]
06	5	-	-	2500	24.2	76	-	-	13.95
07	1	7.5	6.8	44	15.6	6.15	0.42	3.18	nd[e]
10	2/3/4	16.1	7.7	48	2.9	1.28	0.47	2.25	0.19
11	6	-	9.7	61	30.8	9.9	2.3	18.5	2.32
12[a]	1	nd[d]	7.3	nd[d]	6.7	2.82	1.35	2.62	4.72
14	2/4	21.3	9.9	84	6.6	3.1	0.88	32.8	0.46
15	2/3/4	12.1	8.1	39	5.7	0.73	0.16	0.43	0.25
17	3/4	-	8.6	44	6.3	2.82	0.61	34.7	2.41
18	1	8.9	12	41	28.7	6.4	2.82	9.48	nd[e]
20	1	5.1	8.7	196	7.6	11.2	1.94	2.88	5.58
MRed04	1	6.1	8.3	62	3.8	9.61	4.5	5.73	~100
MRed05[a]	2/3/4	15.3	6.1	nd[d]	10	0.17	0.13	0.11	nd[e]
VHH-72[b]	1	59	7.2	490	25	8.46	1.86	9.34	nd[e]
NTD-specific V_HH									
SR01	7/9/10	-	6.6	188	19.5	9.42	3.77	70.3	6.64
SR02	10	-	5.8	nd[d]	11.3	14.13	9.05	~300	9.04
SR03	7/9/10	-	-	269	29.4	~500	22.2	-	~150
SR04	7/9	-	-	-	-	~500	-	-	-
SR13	7/9/10	-	23.8	41	86.9	~100	~100	-	-
SR16	7/9/10	-	-	-	17.5	54.2	17.8	100	-
MRed03	8	-	-	-	-	-	-	-	-
MRed06	8	-	-	-	-	-	-	-	-
MRed07	9	-	-	-	-	-	-	-	-
S2-specific V_HH									
S2A3	11	-	-	nd[d]	-	12.2	31	54	5.36
S2A4	12	-	-	-	-	-	-	-	-
S2F3	13	-	-	nd[d]	-	-	-	-	-
S2G3	14	-	-	-	-	~200	-	-	-
S2G4	15	-	-	-	-	~200	-	-	-
MRed11	16	-	-	-	-	-	-	-	-
MRed18	13	-	-	-	-	-	~400	-	-
MRed19	13	-	-	-	-	-	-	-	-
MRed20	13	-	-	-	-	-	-	-	-
MRed22	13	-	-	-	-	-	-	-	nd[e]
MRed25	17	-	-	-	-	-	-	-	-

[a]The neutralization potencies of nanobodies 12 and MRed05 were not assessed in their V_HH format due to insufficient expression.
[b]VHH-72 benchmark is SARS-CoV S-specific V_HH that cross-reacts with SARS-CoV-2 S[30].
[c]SVNA, PVNA, LVNA, surrogate, pseudo-typed, and live virus neutralization assay, respectively.
[d]nd, not determined (lack of sufficient quantities of V_HHs precluded their assessment for neutralization capabilities).
[e]nd, not determined since they were negative for binding to Omicron S and as a results were not assayed for Omicron neutralization capabilities. Dash indicates lack of neutralization.

assay (LVNA) that employed the Wuhan strain (Fig. 4a; Table 2; and Supplementary Fig. 16). However, compared to the former method, the LVNA IC_{50} values were lower and more variable. For RBD-specific V_HH-Fcs an IC_{50} (range: 0.0008–76 nM; median: 2.8 nM) was observed. The most potent V_HH-Fcs belonged to bin 2/3/4 (IC_{50} range: 0.0008–3.1 nM; median: 1 nM), with V_HH-Fc 05 showing the greatest potency (IC_{50}: 0.0008 nM) followed closely by 02 and MRed05 (IC_{50}s: 0.12 and 0.17 nM, respectively). Bin 1 neutralizers, to which VHH-72 belonged and displayed a similar IC_{50} (8.5 nM), exhibited intermediate potencies (range: 1.9–11.2 nM; median: 6.3 nM), followed by bin 5/6 neutralizers (range: 9.9–76 nM; median: 58 nM). Weaker neutralizing potencies were observed with NTD-specific V_HH-Fcs. Here, six of nine V_HH-Fcs, representing three epitope bins, were neutralizing. Interestingly, three new neutralizers emerged from the pool of S2-specific V_HH-Fcs using the LVNA, with S2A3 the most potent.

The LVNAs were extended to include Alpha and Beta variants. With the exception of V_HH-Fc 06, all remaining 16 RBD-specific Wuhan neutralizers maintained their ability to neutralize Alpha (Table 2; Fig. 4c; and Supplementary Fig. 17). Interestingly, many V_HHs from across different epitope bins showed improved IC_{50}s by as high as 15-fold. Except for 05, which despite showing a reduced potency toward the Alpha variant (~40-fold) still exhibited the highest potency of all against the variant, the remaining V_HHs demonstrated comparable potencies. Of the 16 Wuhan/Alpha neutralizers, 13 also neutralized the Beta variant, with the majority (10 of 13) demonstrating comparable potencies and two (14 and 17) showing reductions (~10-fold). Although from the most potent bin (2/3/4), 02, 04 and 05, consistent with

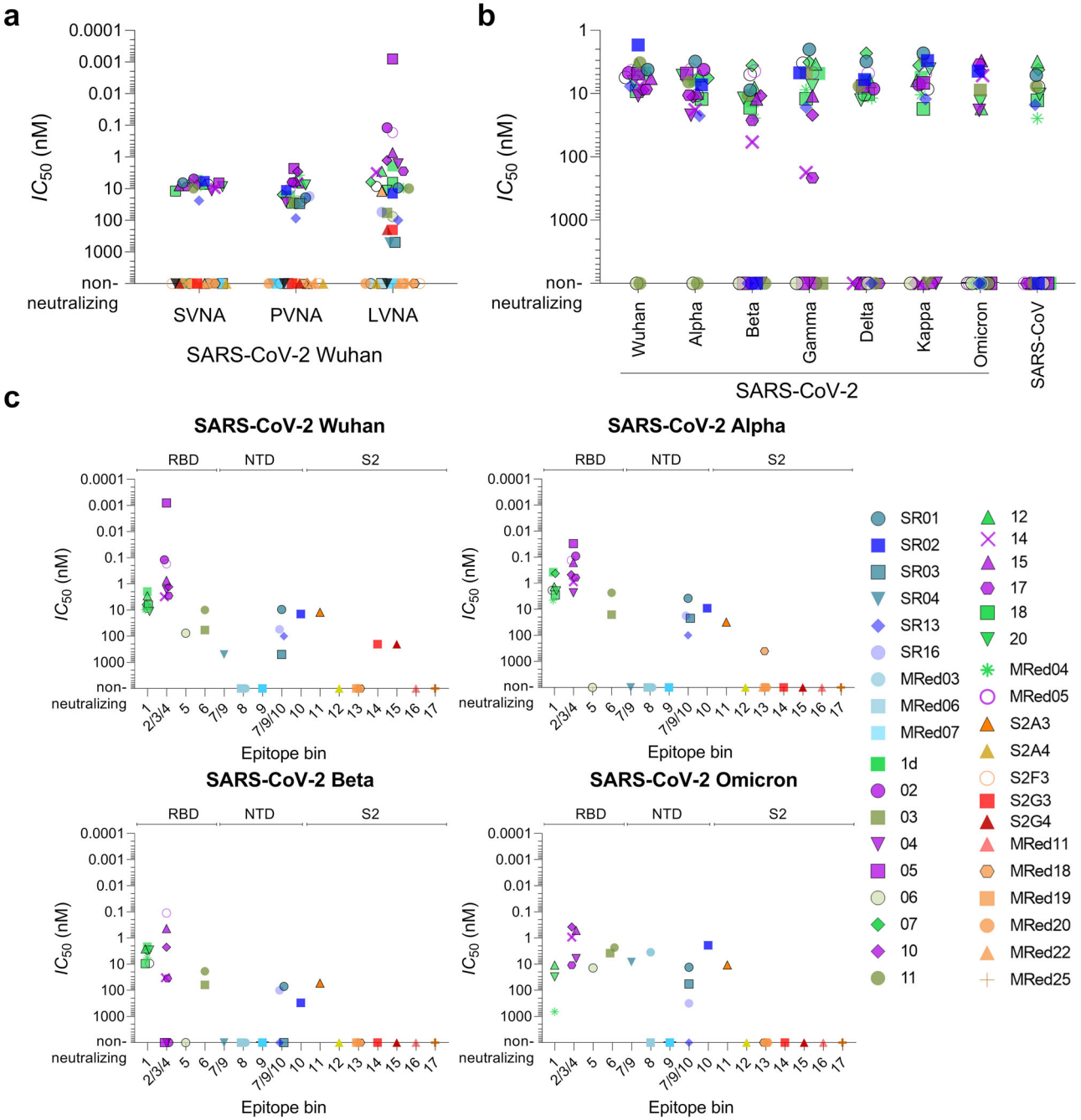

Fig. 4 In vitro neutralization potency of anti-SARS-CoV-2 S V_HH-Fcs. a Summary of IC_{50}s obtained by surrogate (SVNA), pseudotyped (PVNA) and live (LVNA) virus neutralization assays against SARS-CoV-2 Wuhan. **b** Summary of IC_{50}s obtained by SVNAs against SARS-CoV-2 variants Wuhan, Alpha, Beta, Gamma, Delta, Kappa and Omicron (B.1.1.529) and SARS-CoV. **c** Summary of IC_{50}s obtained by LVNAs for V_HH-Fcs against Wuhan, Alpha, Beta and Omicron SARS-CoV-2 variants. See also Table 2 for IC_{50} values. For Omicron LVNAs, only V_HH-Fcs which were positive for binding to Omicron S by ELISA (*see* Fig. 2a) were included. Graphs were generated based on the data in Supplementary Figs. 14–18 and Supplementary Table 8. Black open circle, VHH-72 benchmark. V_HHs are color-coded based on their epitope bin designation (*see* Fig. 1d).

the cross-reactivity data (Fig. 2a), were completely abrogated presumably by the Beta mutations in the RBD (K417N, E484K, and N501Y), several others including MRed05, 10 and 15 did retain their high neutralizing potencies against both Alpha and Beta variants. A similar trend was observed for the NTD-specific neutralizing V_HHs: against the Alpha variant, potencies either remained essentially the same as those for the Wuhan variant or improved, while against the Beta variant, potencies diminished. Nonetheless, SR01 and SR16 maintained considerable neutralization potencies against Beta. The potencies of S2-specific neutralizers (S2A3, S2G3, and S2G4) were also decreased with variants. However, the lead S2A3 still maintained comparable potencies across all three variants (IC_{50} of 12.2 nM, 31 nM and 54 nM for Wuhan, Alpha and Beta [Table 2]).

V_HH-Fcs which were positive for binding to Omicron S (Fig. 2a) were subjected to LVNAs using the most recently emerged Omicron VoC. Fifteen V_HH-Fcs (11 RBD V_HHs, 3 NTD V_HHs, including SR01 and one S2 V_HH [S2A3]) were found to neutralize Omicron, with the majority (13 V_HH-Fcs) demonstrating high potencies (Table 2; Fig. 4c; and Supplementary Fig. 18).

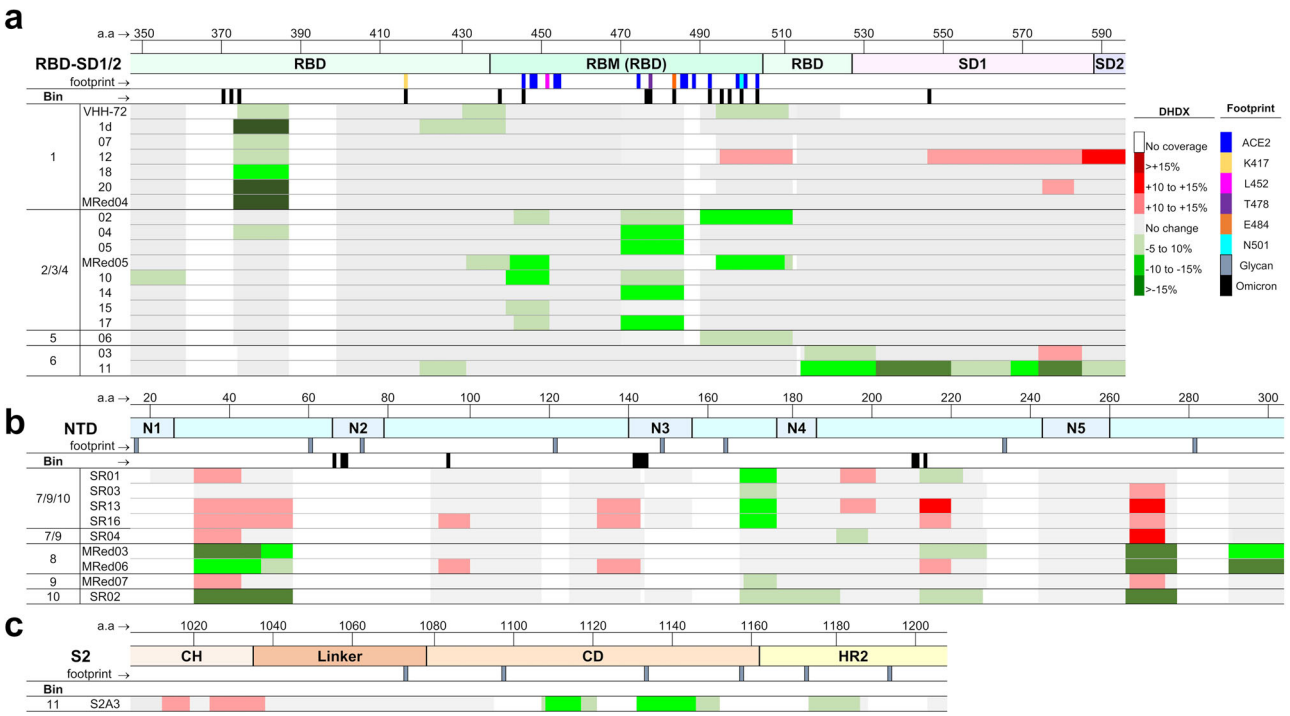

Fig. 5 Epitope mapping. a–c HDX/MS epitope mapping of V_HHs binding RBD (**a**), NTD (**b**) and S2 (**c**). Only relevant S2 residues are shown. Changes in deuteration are mapped as colored rectangles corresponding to primary sequences. Stabilizations are shown in green, and destabilizations are shown in red, while regions with no significant changes in deuteration are shown in gray and missing coverage in white. Key structural features are highlighted by lines below the amino acid sequence, including the ACE2 binding site (blue), mutations from VoCs, and N-linked glycans are included for reference. Source data used to generate the figure are included in Supplementary Data 1.

Collectively, the neutralization profiles across Wuhan, Alpha, Beta and Omicron variants were consistent with cross-reactivity profiles (Fig. 2a). Based on the cross-reactivity (Fig. 2a) and surrogate cross-neutralization data (Fig. 4b and Supplementary Table 8), it is likely that many V_HHs would also neutralize the Gamma, Kappa and Delta variants in LVNAs.

Epitope mapping and typing. We investigated the conformational nature of the epitope bins at peptide-level resolution with hydrogen-exchange mass spectrometry (HDX-MS; Supplementary Table 9) for all RBD and NTD V_HHs and the lead S2 neutralizer S2A3. A summary of normalized HDX shifts are shown in Fig. 5, and projected onto 3-D structures in Supplementary Fig. 19. There is a strong agreement between HDX-MS profiles and previously described epitope bins and subunit/domain specificity. A common binding mode adjacent to the RBM and distant from known VoC mutations was observed for bin 1 (Fig. 5a). This overlaps with core binding contacts of VHH-72 on SARS-CoV[30] where neutralization is achieved by steric blocking of ACE2. The binding profiles for the strongest neutralizers in bins 2/3/4 overlap the ACE2 binding site[11] and known conformational hotspots[60]. It was not possible to further resolve epitope diversity within the context of this dataset, however it is evident that a range of binding patterns exists[61,62], and there is a correlation between stabilizations spanning mutations in VoCs and the loss/attenuation of neutralization (Fig. 5a). Such granularity assists in understanding and predicting neutralization potency as novel variants emerge.

Epitopes for bin 6 (V_HH 03 and 11) span the C-terminus of the RBD and SD1[63] (Fig. 5a), explaining why binding is limited to constructs containing SD1 (Supplementary Table 2). Stabilization of the SD1 hinge responsible for RBD motion highlights a potential inhibitory mechanism for V_HH 11[63]. Although it is challenging to delineate between an epitope and conformational effects based on HDX profiles alone, distinct binding responses with common conformational hotspots were observed for the NTD binders (Fig. 5b and Supplementary Fig. 19). Interestingly, none of the NTD-supersite loops[15–18,20,64–66] covered here displayed significant HDX shifts, except for N4 stabilized by SR02, suggesting a range of binding modes beyond the NTD-supersite. Further, stabilizations partially overlap a previously described conformationally active epitope with low variability and neutralization vulnerability[16]. Supersite binders appear to be vulnerable to escape mutants[7,16,67], highlighting the importance of targeting and characterizing alternative NTD epitopes.

An epitope for S2A3 spanning the linker/CD/HR2 motifs[22] is described in Fig. 5c. This region is upstream of known S2 epitopes and is crucial for the structural transition required for virus-cell fusion[7]. We cannot rule out the involvement of other residues within CD/HR2 regions due to gaps in coverage. Given that none of the mutations within the six SARS-CoV-2 variants overlap the epitope, the cross-reactivity against the six variants (Fig. 2a) and cross-neutralization against Alpha, Beta and Omicron (B.1.1.529) (Table 2), we predict similar neutralization potencies against the Gamma, Kappa, and Delta variants.

Finally, epitope typing by denaturing SDS-PAGE and western blotting indicated 13 of the 37 V_HHs were recognizing linear epitopes, with the majority (9 out of 12) being S2-specific (Table 1 and Supplementary Fig. 20).

In vivo therapeutic efficacy of V_HH-Fcs. Bivalent V_HH-Fcs were chosen over monovalent V_HHs for animal studies because they are characterized by prolonged in vivo serum half-lives and showed much higher in vitro neutralization potencies[68,69], and were thus anticipated to demonstrate enhanced in vivo therapeutic efficacies in animal studies. The in vivo therapeutic efficacy of V_HH-Fcs which were neutralizing by LVNA were assessed

in a hamster model of SARS-CoV-2 infection. Five V_HH-Fcs were selected to cover a wide range of important attributes including in vitro neutralization potencies and breadth, epitope bin, subunit/domain specificity and cross-reactivity pattern. These included three RBD-specific (1d, 05, MRed05), one NTD-specific (SR01) and one S2-specific (S2A3) V_HH-Fcs. Cocktails of two V_HH-Fcs were also included to explore synergy between the antibody pairs recognizing distinct epitopes within the RBD (1d/MRed05) or RBD and NTD (1d/SR01).

Hamsters were administered IP with 1 mg of V_HH-Fcs 24 h before intranasal challenge with SARS-CoV-2 Wuhan isolate. Daily weight change and clinical symptoms were monitored. At 5 dpi, lungs were collected to determine viral titers. Viral titer decrease and reversal of weight loss in antibody treated *versus* control animals were taken as measures of antibody efficacy. Animals treated with RBD binders 1d, 05, and MRed05 showed reduced lung viral burden by three, five and six orders of magnitude, respectively, relative to PBS or V_HH-Fc isotype controls, with 05 and MRed05 reducing viral burden to below detectable levels (Fig. 6a). The RBD-specific VHH-72 benchmark caused a mean viral decrease of four orders of magnitude. The NTD binder SR01, and interestingly, the S2 binder S2A3, were also effective neutralizers, decreasing mean viral titers by four and three orders of magnitude, respectively. Both 1d/SR01 and 1d/MRed05 cocktails decreased viral titers by 6 orders of magnitude to undetectable levels of virus infection. Although it was not possible to unravel potential synergies for 1d/MRed05, as MRed05 alone displayed essentially the same efficacy as the 1d/MRed05 combination, it was apparent that the 1d/SR01 combination benefited from synergy, decreasing viral titers by a further 2–3 orders of magnitude to undetectable levels, relative to 1d or SR01 alone. Moreover, in accordance with the viral titer decreases, a gradual reversal of weight loss in infected animals was observed with antibody treatment starting on 2 dpi (Fig. 6b, c). A strong negative correlation ($r = -0.9436$; $p < 0.0001$) was observed between weight change and viral titer at 5 dpi (Fig. 6d).

Subsequent immunohistochemistry studies corroborated the viral titer and weight change results. First, in agreement with the viral titer observations, substantial viral antigen (nucleocapsid) reductions in hamster lungs were observed with antibody treatments (Fig. 6e; compare non-treated PBS and isotype controls to treated profiles). Although, small foci of viral antigen expression were detected in VHH-72-, 1d-, SR01-, and S2A3-treated animals, none were detected in 05-, MRed05-, 1d/SR01-, and 1d/MRed05-treated animals. Second, SARS-CoV-2 infection is characterized by an overt inflammatory response in the respiratory tract accompanied by an increased infiltration of inflammatory immune cells, e.g., macrophages and T lymphocytes, in the lung parenchyma[70]. As expected, this was the case for the non-treated PBS and isotype control groups. In contrast, we observed a substantial reduction of macrophages and T lymphocytes infiltrate in lung parenchyma with antibody treatment (Supplementary Figs. 21–22). The most dramatic decreases in the number of macrophages and T lymphocytes were seen with 05, MRed05, 1d/MRed05 and 1d/SR01 treatments. Interestingly, a reduction in inflammatory responses was also associated with a decrease in the number of apoptotic cells in antibody-treated animals (Supplementary Fig. 23). Altogether, the viral titer, weight change and immunohistochemistry results consistently demonstrate that a single dose of several of our V_HH-Fcs reduced viral burden, immune cell infiltration, and apoptosis in the lungs of infected hamsters.

Discussion

With the goal of developing broad-spectrum therapeutics, we employed multiple immunization, phage display library construction and panning strategies to identify a diverse collection of SARS-CoV-2-specific nanobodies. These were extensively characterized as monomeric V_HHs and homodimeric V_HH-Fcs. Nanobodies were shown to have high intrinsic affinity (single-digit nM-pM); high thermal, thermodynamic and aerosolization stability; broad epitopic diversity falling into 17 different epitope clusters, broad subunit/domain specificity, recognizing NTD, RBD, and S2 regions; broad cross-reactivities recognizing up to 12 different Sarbecoviruses including several SARS-CoV-2 VoCs and high and broad in vitro virus neutralization potencies. A select set of Fc-fused nanobodies showed high neutralization efficacies in hamster models of SARS-CoV-2 infection, reducing viral burden by up to six orders of magnitude to below detectable levels. Based on published results and our studies, diverse neutralization mechanisms of action can be envisaged for the anti-spike glycoprotein V_HHs, including inhibiting the ACE2-RBD interaction by direct competition, steric hindrance, locking the RBDs in the closed conformation and distorting the RBM, leading to inhibition of the virus-cell binding (RBD- and NTD-specific V_HHs)[4,71–73] and inhibiting conformational rearrangements leading to inhibition of virus-cell fusion (NTD- and S2-specific V_HHs)[16–18,74].

Our study also provides valuable insights into how various in vitro neutralization assays predict antibody efficacy. The flow cytometry-based SVNA was shown to effectively identify neutralizing antibodies that were RBD-specific, providing a viable alternative to the PVNA or LVNA, which are labor-intensive, difficult to standardize, inconvenient and not readily accessible as they require operating in biosafety level 2 or 3 labs. However, the SVNA occasionally missed NTD-specific neutralizing antibodies, and, similar to the PVNA, failed altogether to identify neutralizing antibodies that were S2-specific. Furthermore, the SVNA did not have the sensitivity of the LVNA to identify V_HHs with weaker potencies or, similar to the PVNA, to fine-rank neutralizing antibodies. Since the SVNA identifies neutralizing antibodies based on their ability to interfere with the ACE2-RBD interaction, it is plausible that it primarily identify RBD-specific neutralizing antibodies and to a lesser extent NTD-specific neutralizing antibodies that indirectly interfere with the ACE2-RBD interaction through steric hindrances and/or induction of conformational changes in the RBD. LVNA, on the other hand, identifies neutralizing antibodies based on their ability to interfere with the ACE2-RBD-binding step and/or fusion step which involves the S2 subunit, and thus, it can additionally identify neutralizing antibodies that are S2-specific. It is not clear to us why the PVNA did not identify the S2-specfic neutralizing nanobodies. Inconsistencies between PVNA and LVNA results (i.e., non-neutralizing by PVNA vs neutralizing by LVNA) are not uncommon and may be related to the differences in the presentation of the spike protein during the cell entry step between the live SARS-CoV-2 and pseudotyped SARS-CoV-2 which in turn may be caused by differences in density and geometry of the spike proteins on the surface of the viruses as well as the host cells used in the neutralization assays[20,75]. These differences may have led to the alteration of the cell entry mechanisms for the pseudotyped viruses and preferentially and adversely affected the identification S2-specific neutralizing nanobodies in PVNAs.

For several reasons, the number of epitope bins (17) identified in the current study likely under-estimates the number of actual distinct epitopes. First, V_HHs that recognize (i) partially overlapping epitopes, (ii) fully overlapping epitopes of significantly different nature, or (iii) non-overlapping epitopes, but manifest exclusive binding as a consequence of conformational competition or steric clashes between the V_HH pairs, would fall under the same epitope bins. Second, indicators of distinct epitopes such as

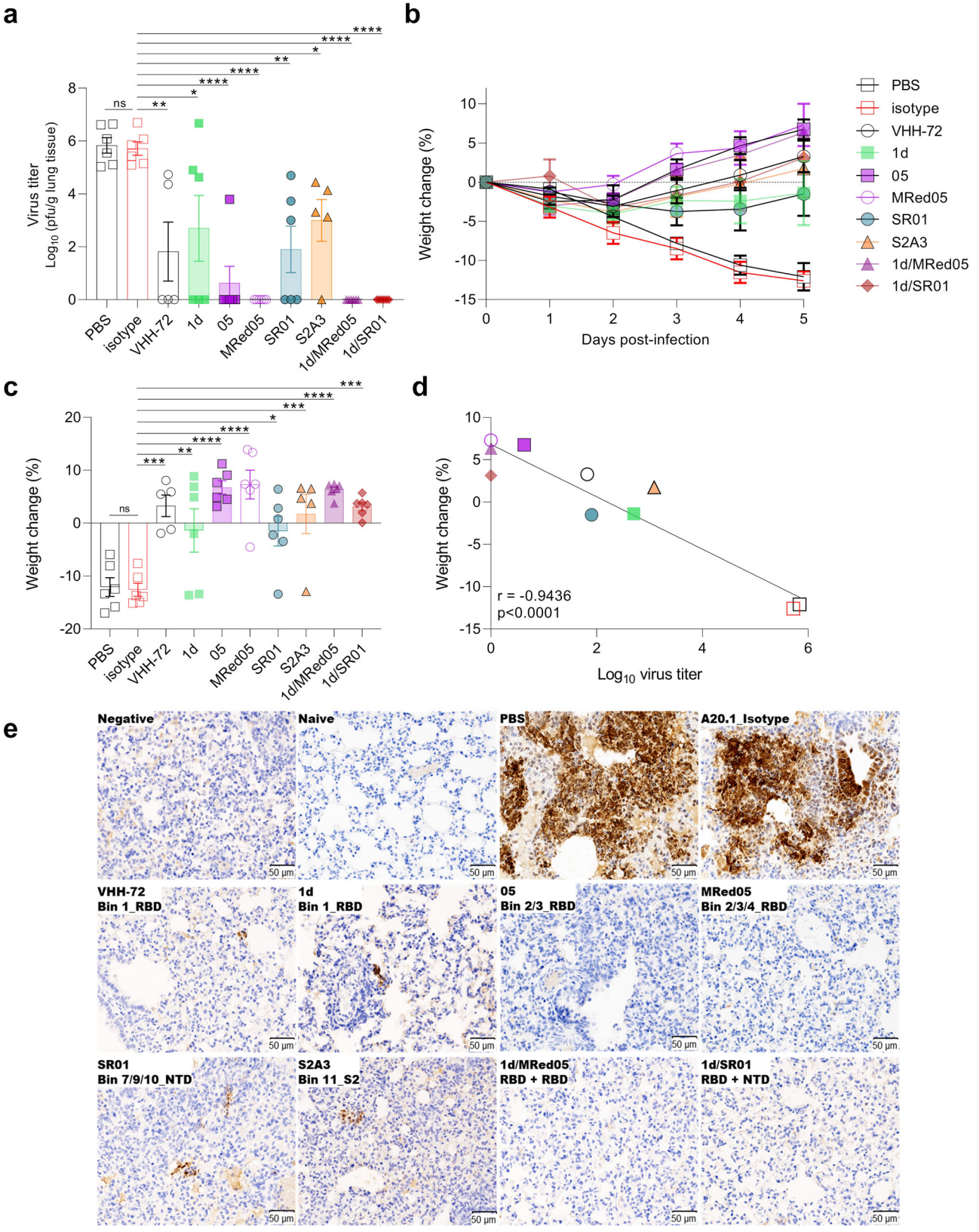

differential HDX-MS footprints, epitope types, cross-reactivity profiles, neutralization potencies, and cross-neutralization profiles not accounted for by affinity alone, are seen amongst V_HHs within the same bin. Thus, the repertoire of structurally and functionally distinct epitopes are more diverse than what can be gleaned from epitope binning analysis alone.

The identification of epitope bins in the current study also provides a useful framework for discussing the roles of different spike epitopes in antibody-mediated protection/neutralization. The SARS-CoV-2 infection process principally relies on the binding of the S1 RBD – more specifically its RBM – to ACE2. Therefore, it is not surprising that the most potent neutralizing

Fig. 6 V_HH-Fcs showed strong protective efficacy in hamsters challenged with SARS-CoV-2. a Lung viral load in V_HH-Fc-treated (VHH-72 benchmark, 1d, 05, MRed05, SR01, S2A3, 1d/MRed05, 1d/SR01) and control groups treated with PBS or isotype A20.1 V_HH-Fc at 5 dpi. pfu, plaque-forming unit. **b** Percent body weight change for antibody-treated and control groups. **c** Percent body weight change at 5 dpi. Error bars indicate standard error of mean (SEM) of five (VHH-72, S2A3) or six (PBS, isotype, 1d, 05, MRed05, SR01, 1d/MRed05, 1d/SR01) biological replicates (animals). In **a** and **c**, treatment effects, assessed by one-way ANOVA with Dunnett's multiple comparison post hoc test, were significant (*$p < 0.05$, **$p < 0.01$, ***$p < 0.001$ or ****$p < 0.0001$). Dunnett's test was performed by comparing treatment groups against the isotype control. ns, not significant. **d** Correlation curve of body weight change vs viral titer at 5 dpi. A strong negative correlation ($r = -0.9436$, $p < 0.0001$) between body weight change and lung viral titer was observed. The exact p-values and the source data used to generate Fig. 6a–d are included in Supplementary Data 1. **e** Immunohistochemical demonstration of SARS-CoV-2 nucleocapsid (N) protein in the lungs of V_HH-Fc-treated animals. Untreated (PBS) and A20.1 isotype-treated animals showed strong viral N protein immunoreactivity which was mainly found in large multifocal patches of consolidated areas. Black arrow indicates the presence of viral N protein in bronchiolar epithelial cells. Omission of anti-nucleocapsid antibody eliminated the staining (Negative). Shown also is the absence of staining in healthy animals (Naïve). A marked reduction in viral N protein staining was seen in all lung tissues examined from V_HH-Fc-treated animals (middle and bottom panels). While no staining was observed in 05, MRed05, 1d/SR01 and 1d/MRed05, small foci of viral N protein was detected in VHH-72, 1d, SR01 and S2A3. Representative images are shown from a single experiment.

antibodies (tested against the Wuhan strain) targeted the RBD epitopes, followed by intermediate-potency antibodies that bound to the RBD-proximal epitopes (S1 NTD epitope bins), with the least potent neutralizing antibodies binding to the RBD-distal epitopes (S2 epitope bins). Within the RBD epitope bins, bin 2/3/4 epitopes gave rise to the most potent neutralizing nanobodies. Bin 1 epitopes produced neutralizing nanobodies with intermediate potencies followed by bin 5 and 6 epitopes which gave the least potent neutralizers. These results are plausible given that based on the HDX-MS results, bin 2/3/4 epitopes overlap the RBM, whereas bin 1 and 6 epitopes are away from the RBM. Furthermore, bin 2/3/4 epitopes spanned known VoC mutations while bin 1 and 6 epitopes were distant from the VoC mutations. Consistently, the neutralizing potencies of antibodies targeting bin 2/3/4 epitopes were most affected with mutations in VoCs, indicating these epitopes compared to bin 1 and 6 epitopes were less conserved across variants. For NTD epitope bins, the neutralizing epitopes were either in bin 7/9/10 (four nanobodies) or bin 10 (one nanobody), with bin 7/9/10 neutralizers showing variable potency and breadth, underlining, as previously mentioned, the subtle but substantial differences that can exist for epitopes within the same bin. In particular, SR01 and SR02 nanobodies, of epitope bins 7/9/10 and 10, respectively, neutralized all current VoCs, with comparable potencies for most variants, indicating their epitopes were highly conserved across VoCs. Of the seven epitope bins identified in S2, only bin 11 presented a substantially neutralizing epitope. S2A3, the lone member of this epitope bin, demonstrated similar neutralization potencies across all VoCs, indicating the conserved nature of its epitope. The knowledge of epitope bin and breadth can be used to combine specificities, in the form of antibody cocktails or multispecific antibodies, for the development of broad-spectrum COVID-19 therapeutics.

In vitro neutralization assays with the Wuhan SARS-CoV-2 variant showed that the majority of the nanobodies were RBD-specific. Importantly, and to our knowledge for the first time, we demonstrated that several NTD- and S2-specific V_HHs were also potent and efficacious neutralizers in vitro and in vivo. However, what makes these V_HHs unique is their format rather than the recognition of NTD and S2, since neutralizing mAbs that also recognize NTD and S2 have been reported[15–22]. Importantly, neutralizing nanobodies showed high epitopic diversity, originating from at least nine different epitope clusters. A proportion of these V_HHs - including NTD and S2 V_HHs - remained potent in vitro neutralizers against the Alpha, Beta, Gamma, Delta, Kappa, and Omicron variants as well, indicating that these nanobodies may bind to cryptic epitopes conserved across variants. A sample of in vitro neutralizing nanobodies, representing RBD-, NTD-, and S2-specific V_HHs, were also shown to be efficacious in vivo neutralizers as single V_HH-Fcs or as paired combinations of V_HH-Fcs that targeted RBD and NTD, with some capable of complete viral clearance from hamster lungs. The IgG1 Fc format of the nanobodies may have additional effector functions that contribute to reduced viral loads/protection in hamsters. This is corroborated in studies where an Fc-enhanced, non-neutralizing mAb delayed virus spread and death in SARS-CoV-2-challenged mice[76] and Fc mutations that compromised Fc-mediated effector functions of neutralizing antibodies also significantly reduced their capacity to protect mice from a lethal SARS-CoV-2 challenge[77]. Our results also confirm the strong positive correlation between the in vitro and in vivo neutralization data and indicate that the remaining in vitro neutralizers might also be in vivo neutralizers. Moreover, given the broad cross-reactivity and cross-neutralization profiles of many of these nanobodies, it is possible that the pan-reactive antibodies may also effectively neutralize emerging VoCs. While cross-reactivity data against several non-SARS-CoV-2 viruses are significant, in the absence of functional studies and given the propensity of RNA viruses to mutate, it remains to be seen how effective these nanobodies will counteract non-SARS-CoV-2 coronaviruses.

With an abundance of neutralizing nanobodies on hand, many possibilities exist for designing optimized multimeric/multiparatopic therapeutic agents. A recent study showed that the neutralization capability of a nanobody significantly increased when fused to a second, non-neutralizing nanobody in a biparatopic format[38]. Thus, the pool of V_HHs can be expanded to include the entire panel of neutralizing and non-neutralizing nanobodies in the current study, leading to a significant number of multimer possibilities. Including the same or similar (same epitope bin) nanobodies in a multimer construct is plausible given the trimeric nature of the spike glycoprotein and its repetitive presentation on the surface of the virus which should accommodate avid inter-protomer, intra-spike, and/or inter-spike binding events. This is supported by the current data showing increased in vitro neutralization potency of nanobodies with homodimerization. CryoEM structures of nanobody-spike glycoprotein complexes would reveal the relative positioning of nanobodies on the surface of the spike glycoprotein and could be used as a guide for designing highly effective and broad-spectrum therapeutic multimers. A comprehensive, high-throughput campaign involving small scale expression of multimers followed by in vitro screening for broad neutralization can also be envisaged.

Furthermore, the ability to aerosolize our V_HHs provides the prospects of a cost-effective, patient-friendly, direct, and effective delivery of therapeutic nanobodies to the nasal and lung epithelia by inhalation[40,41,50–52,78], although it remains to be shown if V_HHs provide in vivo protection by inhalation or V_HH-Fcs can also be aerosolized for inhalation delivery. In addition, the

nanobodies can potentially be utilized to develop detection/diagnosis systems of desired cross-reactivity specifications. Epitope type diversity provides further flexibility for virus detection/diagnosis under native and/or denaturing conditions.

Methods

Recombinant antigens and ACE2. Purified recombinant spike and ACE2 proteins used in the current study are described in Supplementary Table 1. They were either purchased or produced in-house as described (Supplementary Table 1)[13,79–83]. Proteins were purified using standard immobilized metal-ion affinity chromatography (IMAC) or protein A affinity chromatography.

Antigen validation. (a) Binding to cognate human angiotensin-converting enzyme (ACE2) receptor. ELISA was performed to determine if spike glycoprotein fragments (Wuhan) were able to bind to human ACE2 when passively adsorbed (S, S1, RBD and S2) or directionally captured (S1, RBD) on microtiter wells. For passive adsorption, wells of NUNC® Immulon 4 HBX microtiter plates (Thermo Fisher, Ottawa, Canada, Cat#3855) were coated with 50 ng of SARS-CoV-2 spike proteins (S, S1, S2, RBD) in 100 µL of phosphate-buffered saline (PBS) overnight at 4 °C. Following removal of protein solutions and three washes with PBST (PBS supplemented with 0.05% [v/v] Tween 20), wells were blocked with PBSC (1% [w/v] casein [Sigma, Oakville, Canada, Cat#E3414] in PBS) at room temperature for 1 h. For capturing, in vivo biotinylated fragments harboring the AviTag™ (AviTag-S1, AviTag-RBD) were diluted in PBS and added at 50 ng/well (100 µL) to pre-blocked Streptavidin Coated High Capacity Strip wells (Thermo Fisher, Cat#15501). After 1 h incubation at room temperature, wells were washed five times with PBST and incubated for an additional hour with 100 µL/well of 2-fold serially diluted ACE2-Fc (human ACE2 fused to human IgG1 Fc; ACROBiosystems, Newark, DE, Cat#AC2-H5257) in PBSTC (PBS/0.2% casein/0.1% Tween 20). Wells were washed five times and incubated for 1 h with 1 µg/mL HRP-conjugated goat anti-human IgG (Sigma, Cat#A0170). Finally, wells were washed 10 times and incubated with 100 µL peroxidase substrate solution (SeraCare, Milford, MA, Cat#50-76-00) at room temperature for 15 min. Reactions were stopped by adding 50 µL 1 M H_2SO_4 to wells, and absorbance were subsequently measured at 450 nm using a Multiskan™ FC photometer (Thermo Fisher). (b) Binding to cognate anti-spike glycoprotein polyclonal antibody. The four spike glycoprotein antigens were passively adsorbed as described above. After blocking with PBSC, wells were emptied, washed five times with PBST and incubated at room temperature for 1 h with 100 µL of 1 µg/mL anti-SARS-CoV-2 spike rabbit polyclonal antibody (Sino Biological, Beijing, China, Cat#40589-T62) in PBSTC. Following 10 washes with PBST, wells were incubated with 100 µL 1/2500 dilution (320 ng/mL) of goat anti-rabbit:HRP (Jackson ImmunoResearch, West Grove, PA, Cat#111-035-144) in PBSTC for 1 h at room temperature. After 1 h incubation and final five washes with PBST, the peroxidase activity was determined as described above.

Llama immunization and serum analyses. (a) Llama immunization. Immunizations of 2 four-year-old female llamas (*lama glama*) were performed at Cedarlane Laboratories (Burlington, Canada) essentially as described[84,85], using SARS-CoV-2 Wuhan spike glycoprotein fragments. Briefly, for priming, both llamas (Green and Red) were injected with 100 µg of S in 500 µL PBS combined with 500 µL of Freund's Complete Adjuvant. For the three subsequent boosts (days 7, 14, 21), Green was injected with 70 µg of RBD (ACROBiosystems, Cat#SPD-S52H6) whereas Red received 100 µg of S[83] at day 7 and 50 µg of S on days 14 and 21 all with Freund's Incomplete Adjuvant. Experiments involving animals were conducted using protocols approved by the National Research Council Canada Animal Care Committee and in accordance with the guidelines set out in the OMAFRA Animals for Research Act, R.S.O. 1990, c. A.22. (b) Serum ELISA. Llama sera were tested for antigen-specific immune response by ELISA essentially as described[85,86]. Briefly, dilutions of sera in PBST were added to wells pre-coated with S, S1, S2, or RBD. Negative antigen control wells were pre-coated with casein (100 µL of 1%). Following 1 h incubation at room temperature, wells were washed 10 times with PBST and incubated with HRP-conjugated polyclonal goat anti-llama IgG heavy and light chain antibody (Bethyl Laboratories, Montgomery, TX, Cat#A160-100P) for 1 h at room temperature. After 10 washes, the peroxidase activity was determined as described in section "Antigen validation". (c) Serum surrogate neutralization assay by flow cytometry. SARS-CoV-2 S was chemically biotinylated using EZ-Link™ NHS-LC-LC-Biotin following manufacturer instructions (Thermo Fisher, Cat#21343). Vero E6 cells (ATCC, Cat#CRL-1586) were maintained according to ATCC protocols. Briefly, cells were grown to confluency in DMEM medium (Thermo Fisher, Cat#11965084) supplemented with 10% (w/v) heat inactivated fetal bovine serum (FBS; Thermo Fisher, Cat#10438034) and 2 mM Glutamax (Thermo Fisher, Cat#35050061) at 37 °C in a humidified 5% CO_2 atmosphere in T75 flasks. For flow cytometry experiments, cells were harvested by Accutase (Thermo Fisher, Cat#A1110501) treatment, washed once by centrifugation with PBS, and resuspended at 1×10^6 cells/mL in PBSB (PBS containing 1% [w/v] BSA and 0.05% [v/v] sodium azide [Sigma, Cat#S2002]). Cells were kept on ice until use. To determine the presence of antibodies that block the binding of S to ACE2 (surrogate for neutralization) in the immune sera of llamas, 400 ng of chemically biotinylated SARS-CoV-2 S was mixed with 1×10^5 Vero E6 cells in the presence of 2-fold dilutions of sera (pre immune, day 21 and day 28 sera) in a final volume of 150 µL. Following 1 h of incubation on ice, cells were washed twice with PBSB by centrifugation for 5 min at 1200 rpm and then incubated for an additional hour with 50 µL of Streptavidin, R-Phycoerythrin Conjugate (SAPE, Thermo Fisher, Cat#S866) at 250 ng/mL diluted in PBSB. After a final wash, cells were resuspended in 100 µL PBSB and data were acquired on a CytoFLEX S flow cytometer (Beckman Coulter, Brea, CA) and analyzed by FlowJo software (FlowJo LLC, v10.6.2, Ashland, OR). Percent inhibition (neutralization) was calculated according to the following formula:

$$\%\,\text{inhibition} = 100 \times [1 - (F_n - F_{min})/(F_{max} - F_{min})] \quad (1)$$

Where,

F_n is the measured fluorescence at any given competitor serum dilution.

F_{min} is the background fluorescence measured in the presence of cells and SAPE only.

F_{max} is the maximum fluorescence measured in the absence of competitor serum.

Phage display library construction, selection, and screening. (a) Phage display library construction. On day 28, 100 mL of blood from each of the two llamas was drawn and peripheral blood mononuclear cells (PBMCs) were purified by ficoll gradient at Cedarlane Laboratories. Two independent phage-displayed V_HH libraries were constructed from $\sim 5 \times 10^7$ PBMCs as described previously[84,85,87]. Briefly, total RNA was extracted from PBMCs using TRIzol™ Plus RNA Purification Kit (Thermo Fisher, Cat#12183555) following the manufacturer's instructions and used to reverse transcribe cDNA with SuperScript™ IV VILO™ Master Mix supplemented with random hexamer (Thermo Fisher, Cat#SO142) and oligo (dT) (Thermo Fisher, Cat#AM5730G) primers. V_HH genes were amplified using semi-nested PCR and cloned into the phagemid vector pMED1, followed by transformation of *E. coli* TG1 (Lucigen, Middleton, WI, Cat#60502-02) to construct two libraries with sizes of 1×10^7 and 2×10^7 independent transformants for Green and Red, respectively. Both libraries showed an insert rate of ~95% as verified by DNA sequencing. Phage particles displaying the V_HHs were rescued from *E. coli* cell libraries using M13K07 helper phage (New England Biolabs, Whitby, Canada, Cat#N0315S) as described in ref. [84] and used for selection experiments described below. (b) Library selection and screening. Library panning and screening were performed essentially as described[84,85,88], using SARS-CoV-2 Wuhan spike glycoprotein fragments as target antigens. Library selections were performed on microtiter wells under six different phage binding/elution conditions designated P1–P6. Briefly, for the phage binding step, library phages were diluted at 1×10^{11} colony-forming units (CFU)/mL in PBSBT (PBS supplemented with 1% BSA and 0.05% Tween 20) and incubated in antigen-coated microtiter wells for 2 h at 4 °C. For P1–P4, phages were added to wells with passively adsorbed S (10 µg/well; P1), passively adsorbed S2 (10 µg/well; P2), streptavidin-captured biotinylated S1 (0.5 µg/well; P3), and streptavidin-captured biotinylated RBD (0.5 µg/well; P4). For P5, phages were pre-absorbed on passively adsorbed RBD wells (10 µg/well) for 1 h at 4 °C and then the unbound phage in the solution was transferred to wells with streptavidin-captured biotinylated S1 (0.5 µg/well) in the presence of non-biotinylated RBD competitor in solution (10 µg/well). Following the binding stage (P1–P5), wells were washed 10 times with PBST and bound phages were eluted by treatment with 100 mM glycine, pH 2.2, for 10 min at room temperature, followed by immediate neutralization of phages with 2 M Tris. Similar to P4, in P6, phages were bound on streptavidin-captured biotinylated RBD but elution of bound phages were carried out competitively with 50 nM human ACE2-Fc following the washing step. For all pannings, a small aliquot of eluted phage was used to determine the titer on LB-agar/ampicillin plates and the remaining phage were used for subsequent amplification in *E. coli* TG1 strain[84]. The amplified phages were used as input for the next round of selection as described above.

After two rounds of selection, 16 (Green) or 12 (Red) colonies from each of the P1–P6 selections were screened for antigen binding by monoclonal phage ELISA against S, S1, S2, and RBD. Briefly, individual colonies from eluted-phage titer plates were grown in 96 deep well plates in 0.5 mL 2YT media/100 µg/mL-carbenicillin/1% (w/v) glucose at 37 °C and 250 rpm to an OD_{600} of 0.5. Then, 10^{10} CFU M13K07 helper phage was added to each well and incubation continued for another 30 min under the same conditions. Cells were subsequently pelleted by centrifugation, the supernatant was discarded and the bacterial pellets were resuspended in 500 µL 2YT/100 µg/mL carbenicillin/50 µg/mL kanamycin and incubated overnight at 28 °C. Next day, phage supernatants were recovered by centrifugation, diluted 3-fold in PBSTC and used in subsequent screening assays by ELISA. To this end, antigens were coated onto microtiter wells at 50 ng/well overnight at 4 °C. Next day, plates were blocked with PBSC, washed five times with PBSTC, and 100 µL of phage supernatants prepared above were added to wells, followed by incubation for 1 h at room temperature in an orbital shaking platform. After 10 washes, binding of phages was detected by adding 100 µL/well of anti-M13:HRP (Santa Cruz Biotechnology, Santa Cruz, CA, Cat#SC-53004HRP) at 40 ng/mL in PBSTC and incubating as above. After 10 washes, the peroxidase activity was determined as described in section "Antigen validation". After monoclonal phage ELISA confirmed the library panning was successful, a total of ≈1200 clones (≈100 clones per panning strategy; ≈600 clones per library) were

subjected to colony-PCR and DNA sequencing, resulting in the identification of 26 (Green) and 11 (Red) V_HHs.

Expression and purification of V_HHs and V_HH-Fcs. (a) Expression and validation of V_HHs. Positive V_HHs were cloned into a modified pET expression vector (pMRo.BAP.H6) for their production in BL21(DE3) *E. coli* as monomeric soluble protein[87]. For the VHH-72 benchmark[30], the sequence of the V_HH was synthesized as a GeneBlock (Integrated DNA Technologies, Coralville, IA) flanked by SfiI sites for cloning into pMRo.BAP.H6. Briefly, individual colonies were cultured overnight in 10 mL LB supplemented with 50 µg/mL of kanamycin (LB/Kan) at 37 °C and 250 rpm. After 16 h, cultures were added to 250 mL LB/Kan and grown to an OD_{600} of 0.6. Expression of V_HHs was induced with 10 µM of IPTG (isopropyl β-D-1-thiogalactopyranoside) overnight at 28 °C and 250 rpm. Next day, bacterial pellets were harvested by centrifugation at 6000 rpm for 15 min at 4 °C, V_HHs were extracted by sonication and purified by IMAC as described[87]. Protein purity was evaluated by SDS-PAGE using 4–20% Mini-PROTEAN® TGX Stain-Free™ Gels (BioRad, Hercules, CA, Cat#17000435). In addition, for ELISA (*see* below), V_HHs were enzymatically biotinylated in their BAP tag by incubating 1 mg of purified V_HHs with 10 µM of ATP (Alfa Aesar, Haverhill, MA, Cat#CAAAJ61125-09), 100 µM of D-(+)-biotin (VWR, Mississauga, Canada; Cat#97061-446) and bacterial cell extract overexpressing *E. coli* BirA as described[84]. V_HHs were validated for binding by soluble ELISA against spike glycoprotein fragments (S, S1, RBD, NTD, S2). Briefly, microtiter well plates were coated with 50 ng/well SARS-CoV-2 spike glycoprotein fragments in 100 µL PBS overnight at 4 °C. Plates were blocked with PBSC for 1 h at room temperature, then washed five times with PBST and incubated with increasing concentrations of biotinylated V_HHs. After 1 h incubation, plates were washed 10 times with PBST and binding of V_HHs was probed using HRP-streptavidin (Jackson ImmunoResearch, Cat#016-030-084). Finally, plates were washed 10 times with PBST and peroxidase activity was determined as described in section "Antigen validation". (b) Production of V_HHs in mammalian cells in fusion with human IgG1 Fc (V_HH-Fcs). Codon-optimized genes for bivalent V_HH-Fcs were synthesized and cloned into pTT5 (GenScript; Piscataway, NJ). For VHH-72 V_HH-Fc,[30] the sequence of the V_HH was synthetized as GeneBlock (Integrated DNA Technologies) flanked by NarI/HindIII for cloning into pTT5. V_HH-Fcs were produced by transient transfection of HEK293-6E cells followed by protein A affinity chromatography as previously described[87]. Proteins were buffer exchanged using Amicon® Ultra-15 Centrifugal Filter Units (Millipore-Sigma, Oakville, Canada, Cat#UFC905024) with PBS, pH 7.4. Protein purity was evaluated by SDS-PAGE using 4–20% Mini-PROTEAN® TGX Stain-Free™ Gels (BioRad, Cat#17000435).

Affinity and specificity assays. (a) Cross-reactivity assays by ELISA. Recombinant coronavirus spike glycoproteins S (Supplementary Table 1) were coated overnight onto NUNC® Immulon 4 HBX microtiter plates (Thermo Fisher) at 50 ng/well in 100 µL of PBS, pH 7.4. The next day, plates were blocked with 200 µL PBSC for 1 h at room temperature, then washed five times with PBST and incubated at room temperature for 1 h on rocking platform at 80 rpm with 1 µg/mL V_HH-Fc diluted in PBSTC. Plates were washed five times with PBSTC and binding of V_HH-Fcs was detected using 1 µg/mL HRP-conjugated goat anti-human IgG. Finally, plates were washed five times and peroxidase (HRP) activity was measured as described in section "Antigen validation". (b) Affinity/specificity determination of V_HHs against SARS-CoV spike (S), SARS-CoV-2 spike (S) and SARS-CoV/SARS-CoV-2 spike fragments by surface plasmon resonance (SPR). Standard SPR techniques were used for binding studies. All SPR assays were performed on a Biacore T200 instrument (Cytiva, Vancouver, Canada) at 25 °C with HBS-EP running buffer (10 mM HEPES, 150 mM NaCl, 3 mM EDTA, 0.005% Tween 20, pH 7.4) and CM5 sensor chips (Cytiva). Prior to SPR analyses, all analytes in flow (V_HHs, ACE2 receptor) were purified by size exclusion chromatography (SEC) on a Superdex 75™ Increase 10/300 GL column (Cytiva) in HBS-EP buffer at a flow rate of 0.8 mL/min to obtain monomeric proteins. SARS-CoV spike glycoprotein (S), SARS-CoV-2 spike glycoprotein (S)[83] and various SARS-CoV-2 spike glycoprotein fragments were immobilized on CM5 sensor chips through standard amine coupling (10 mM acetate buffer, pH 4.0, Cytiva). On the first sensor chip, 1983 response units (RUs) of SARS-CoV spike (SinoBiological, Cat#40634-V08B), 843 RUs of SARS-CoV-2 RBD/SD1 fused to human Fc (RBD/SD1-Fc) and 972 RUs of EGFR (Genscript, Cat# Z03194, as an irrelevant control surface) were immobilized. On a second sensor chip, 2346 RUs of SARS-CoV-2 S, 1141 RUs of SARS-CoV-2 S1 subunit and 1028 RUs of SARS-CoV-2 S2 subunit were immobilized. A third sensor chip contained 489 RUs of RBD_short[83]. The theoretical maximum binding response for V_HHs binding to these surfaces ranged from 224–262 RUs. An ethanolamine blocked surface on each sensor chip served as a reference. Single cycle kinetics was used to determine V_HH and ACE2 binding kinetics and affinities. V_HHs at various concentration ranges (from 0.25 to 4 nM to 125–2000 nM) were flowed over all surfaces at a flow rate of 40 µL/min with 180 s of contact time and 600 s of dissociation time. Surfaces were regenerated with a 12 s pulse of 10 mM glycine, pH 1.5, at a flow rate of 100 µL/min. Injection of EGFR-specific V_HH NRCsdAb022[87] served as a negative control for the SARS-CoV and SARS-CoV-2 surfaces and as a positive control for the EGFR surface. The ACE2 affinity was determined using similar conditions by flowing a range of monomeric ACE2 concentrations (31.3–500 nM). SARS-CoV-2 spike glycoproteins from Alpha and Beta variants were also tested by SPR and amine coupled using the conditions described above. All affinities were calculated by fitting reference flow cell-subtracted data to a 1:1 interaction model using BIAevaluation Software v3.0 (Cytiva).

For V_HH 12 and MRed05, V_HH-Fc formats were used in SPR experiments. Approximately 200 RUs of V_HH-Fcs (1–2 µg/mL) were captured on goat anti-human IgG Fc surfaces (4000 RUs, Jackson ImmunoResearch, Cat#109-005-098) at a flow rate of 10 µL/min for 30 s. A range of SEC-purified SARS-CoV-2 RBD fragments (Supplementary Table 1; Wuhan[83], Alpha and Beta) at 0.62–10 nM were flowed over the captured V_HH-Fc at a flow rate of 40 µL/min with 180 s of contact time and 300 s of dissociation. A SEC-purified SARS-CoV RBD fragment was also flowed over captured V_HH 12-Fc and MRed05-Fc at 0.62–10 nM and 31.25–500 nM, respectively, at 40 µL/min with 180 s of contact time and 600 s of dissociation. Surfaces were regenerated with a 120 s pulse of 10 mM glycine, pH 1.5, at a flow rate of 50 µL/min. Affinities were calculated from reference flow cell subtracted sensorgrams as described above. (c) Domain specificity determination of V_HHs by ELISA. V_HHs which bound to S1 subunit but not to the RBD domain in SPR assays were further examined by ELISA to determine if they were binding to the NTD domain of S1. Briefly, S, S1, NTD, and RBD were coated onto NUNC® Immulon 4 HBX microtiter plates at 100 ng/well in 100 µL PBS, pH 7.4. Next day, plates were blocked with 200 µL PBSC for 1 h at room temperature, then washed five times with PBST and incubated with fixed (13 nM) or decreasing concentrations of V_HH-Fcs diluted in PBSTC. After 1 h, plates were washed 10 times with PBSTC and binding of V_HH-Fc fusions was detected by incubating wells with 100 µL of 1 µg/mL HRP-conjugated goat anti-human IgG Fc. Finally, plates were washed 10 times with PBST and peroxidase activity was determined as described in section "Antigen validation". EC_{50}s for the binding of V_HH-Fcs to S and S fragments were obtained from the plot of $A_{450\,nm}$ (binding) vs V_HH-Fc concentration. (d) Cell binding assays by flow cytometry. CHO$^{55E1™}$ cells expressing full-length (including transmembrane and C-terminal domains) SARS-CoV-2 Wuhan S (CHO-SPK) under control of the cumate-inducible CR5 promoter were generated by methionine sulfoximine (MSX) selection of plasmid-transfected cells, as described[89]. Cells were grown in BalanCD™ CHO Growth A medium (Irvine Scientific, Santa Ana, CA) supplemented with 50 µM methionine sulfoximine (MSX) at 120 rpm and 37 °C in a humidified 5% CO_2 atmosphere. Expression of S was induced by adding cumate at 2 µg/mL for 48 h at 32 °C. For flow cytometry experiments, cells were harvested by centrifugation and resuspended at 1×10^6 cells/mL in PBSB. Cells were kept on ice until use. Serially, three-fold dilutions of V_HH-Fcs were prepared in V-Bottom 96-well microtiter plates (Globe Scientific, Mahwah, NJ, Cat# 120130) and mixed with 50 µL of CHO-SPK cells. Plates were incubated for 1 h on ice, washed twice with PBSB by centrifugation for 5 min at 1200 rpm and then incubated for an additional hour with 50 µL of R-Phycoerythrin AffiniPure F(ab')$_2$ Fragment Goat Anti-Human IgG (Jackson ImmunoResearch, Cat#109-116-170) at 250 ng/mL diluted in PBSB. After a final wash, cells were resuspended in 100 µL PBSB and data were acquired on a Beckman Coulter CytoFlex S and analyzed by FlowJo™ (FlowJo LLC, v10.6.2). EC_{50}s for the binding of V_HH-Fcs to CHO-SPK cells were obtained from the plot of MFI (Mean Fluorescent Intensity) vs V_HH-Fc concentration.

Stability assays. (a) Determination of aggregation resistance by SEC. Purified V_HHs were subjected to SEC to validate their aggregation resistance. Briefly, 2 mg of each affinity purified V_HH was injected into Superdex™ 75 10/300 GL column (Cytiva) connected to an ÄKTA FPLC protein purification system (Cytiva) as previously described[90]. PBS was used as the running buffer at 0.8 mL/min. Fractions corresponding to the monomeric peak were pooled and stored at 4 °C until use. (b) Thermostability determinations by circular dichroism. To determine thermostability, V_HH T_ms were measured by circular dichroism as previously described[90]. Ellipticity of V_HHs were determined at 200 µg/mL V_HH concentrations and 205 nm wavelength in 100 mM sodium phosphate buffer, pH 7.4. Ellipticity measurements were normalized to percentage scale and T_ms were determined from plot of % folded vs temperature and fitting the data to a Boltzmann distribution. (c) Isothermal chemical denaturation (ICD). All ICD experiments were performed with the automated Hunky system (Unchained Labs, Pleasanton, CA), using Hunky Client software (v1.2). V_HHs were prepared in PBS buffer, pH 7.2 (Teknova, Hollister, CA, Cat#P0191), and diluted by Hunky automation to 20 µg/mL. They were denatured using a linear dilution gradient of 0–5.52 M guanidine·HCl (Sigma, Cat#G3272) and incubated for 2 h at 25 °C. Samples were subjected to LED excitation at 280 nm, and emission spectra of the V_HH were captured by a CCD spectrometer from 300--720 nm. The Hunky Analysis v1.2 Software automatically plotted the fluorescence intensity against denaturant concentration, and generated a data fit curve for two-state transitions of each V_HH. All samples were analyzed by the Hunky software using the Barycentric Mean (BCM) except for 05 (348/342 nm ratio), 06 (single 348 nm), and 07 (wavelength diff. 348-420 nm) to determine ΔG^0 (kJ/mol), C_m (M), and m (kJ/M*mol). The fraction denatured was automatically plotted against denaturant concentration to confirm the two-state model. The denatured-induced unfolding of V_HHs was considered to be reversible based on their small size as shown to be the case for small proteins and numerous times for V_HHs[55,57–59,91,92]. (d) Serum stability. Three six-seven weeks old female LVG Golden Syrian hamsters (90–100 g) were injected intraperitoneally (IP) with 1 mg of 1d or VHH-72

V_HH-Fc diluted in 200 µL PBS. Animal were bled on day 0, 1, and 4 post injection and their sera were subjected to ELISA to detect their V_HH-Fc levels. Briefly, sera were diluted 1/6000, in order to give final A_{450nm} readings of ≤1 in 15 min, and incubated 1 h at room temperature in wells coated with SARS-CoV-2 Wuhan S[83]. The binding of V_HH-Fcs within the sera was detected using 1 µg/mL goat anti-human IgG Fc, HRP-conjugated (Thermo Fisher, Cat#A18829). Plates were washed five times with PBST and peroxidase (HRP) activity was detected as described in section "Antigen validation". The levels of 1d and VHH-72 V_HH-Fcs in sera were quantified by interpolating obtained A_{450nm} readings against A_{450nm} vs [V_HH-Fc] standard curves generated with purified 1d and VHH-72 V_HH-Fcs, respectively. (e) Aerosolization studies. Prior to aerosolization, 4 mg of each V_HH were purified by SEC using a Superdex 75™ 10/300 GL column (Cytiva) and PBS as running buffer, as described above. Protein fractions corresponding to the chromatogram's monomeric peak were pooled, quantified and its concentration adjusted to 0.5 mg/mL. One mL of each V_HH was subsequently aerosolized at room temperature with a portable mesh nebulizer (AeroNeb Solo, Aerogen, Galway, Ireland), which produces 3.4-µm particles. Aerosolized V_HHs were collected into 15 mL round-bottom polypropylene test tubes (VWR, Cat#C352059) for 5 min to allow condensation and were subsequently quantified and kept at 4 °C until use. Then 200 µL aliquots of pre- and post- aerosolized V_HHs were subjected to SEC to obtain chromatogram profiles. Additionally, condensed V_HHs were closely monitored for the formation of any visible aggregates, and in cases where aggregate formation were observed, they were removed by centrifugation prior to concentration determination, SEC analysis and ELISA. Percentage soluble aggregate was determined as the proportion of a V_HH that gave elution volumes (V_es) smaller than that of the monomeric V_HH fraction. % recovery was determined as the proportion of a V_HH that remained monomer following aerosolization.

To assess the effect of aerosolization on functionality of V_HHs, the activities of post-aerosolized V_HHs were determined by ELISA and compared to those for pre-aerosolized V_HHs. To perform ELISA, S1-Fc (ACROBiosystems, Cat#S1N-C5255) was diluted in PBS to 500 ng/mL, and 100 µL/well were coated overnight at 4 °C. Next day, plates were washed with PBST and blocked with 200 µL PBSC for 1 h at room temperature. After five washes with PBST, serial dilutions of the pre- and post- aerosolized V_HHs were added to wells and incubated for 1 h at room temperature. Then plates were washed 10 times with PBST and binding of V_HHs to S1-Fc was detected with rabbit anti-6xHis Tag antibody HRP Conjugate (Bethyl Laboratories, Cat#A190-114P), diluted at 10 ng/mL in PBST and added at 100 µL/well. Finally, after 1 h incubation at room temperature and final washes with PBST, peroxidase (HRP) activity was determined as described in section "Antigen validation".

Epitope typing, binning, and mapping. (a) Epitope typing by sodium dodecyl sulfate-polyacrylamide gel electrophoresis/western blotting (SDS-PAGE/WB). A standard SDS-PAGE/WB was performed to detect the binding of V_HH-Fcs to nitrocellulose-immobilized, denatured SARS-CoV-2 Wuhan S. Briefly, 10 µg/lane of S was run on 4–20% Mini-PROTEAN® TGX Stain-Free™ Protein Gels (BioRad, Cat#4568081), transferred to nitrocellulose (Sigma, Cat#GE10600002) and blocked with 1% PBSC overnight at 4 °C. Then, 0.5-cm nitrocellulose strips containing the denatured S were placed on Mini Incubation Trays (BioRad, Cat#1703902) and incubated with 1 mL of 1 µg/mL V_HH-Fcs. After 1 h incubation at room temperature, strips were washed 10 times with PBST and the binding of V_HH-Fcs to denatured S was probed by incubating strips with 1 mL of 100 ng/mL anti-human IgG Fc antibody-peroxidase conjugate (Sigma, Cat#A0170) at room temperature for 1 h. Finally, strips were washed 10 times with PBST and peroxidase activity was detected using chemiluminescent reagent (SuperSignal West Pico PLUS Chemiluminescent Substrate, Thermo Fisher, Cat#34580). Images of developed strips were acquired on Molecular Imager® Gel Doc™ XR System (BioRad, Cat#1708195EDU). (b) Epitope binning by SPR. Standard SPR techniques were used for binding studies. All SPR assays were performed on a Biacore T200 instrument (Cytiva) at 25 °C with HBS-EP running buffer (10 mM HEPES, 150 mM NaCl, 3 mM EDTA, 0.005% Tween 20, pH 7.4) and CM5 sensor chips (Cytiva). Prior to SPR analyses, all analytes in flow (V_HHs, ACE2 receptor) were SEC-purified on a Superdex 75™ Increase 10/300 GL column (Cytiva) in HBS-EP buffer at a flow rate of 0.8 mL/min to obtain monomeric proteins. V_HH epitope binning was performed by SPR dual injection experiments on the SARS-CoV-2 S surface at a flow rate of 40 µL/min in HBS-EP buffer. Dual injections consisted of injection of V_HH1 (at 50–100 × K_D concentration) for 150 s, followed by immediate injection of a mixture of V_HH1 + V_HH2 (both at 50–100 × K_D concentration) for 150 s. The opposite orientation was also performed (V_HH2 followed by V_HH2 + V_HH1). Surfaces were regenerated using a 12 s pulse of 10 mM glycine, pH 1.5, at a flow rate of 100 µL/min. All pairwise combinations of V_HHs were analyzed and distinct or overlapping epitope bins determined. (c) Epitope binning by ELISA. The pairwise ability of RBD V_HHs to bind to their antigen in a sandwich ELISA format was evaluated as described previously[88,93,94] and according to the design depicted in Supplementary Fig. 6b. Briefly, a matrix of 17 well (row) × 20 well (column) in NUNC® Immulon 4 HBX microtiter plates (Thermo Fisher) was coated overnight at 4 °C with 4 µg/mL streptavidin (Jackson ImmunoResearch, Cat#016-000-113) in 100 µL PBS, pH 7.4. Wells were blocked with 200 µL PBSC for 1 h at room temperature and then biotinylated V_HHs at 10 µg/mL in 100 µL PBSCT were captured in each row (same V_HH in each row; 17 rows for a total of 17 V_HHs) for 1 h at room temperature. Wells were washed 5 times with PBST and incubated with 100 ng/mL of SARS-CoV-2 Wuhan S1 diluted in PBSCT for 1 h. Wells were washed and each column was incubated with the pairing, V_HH-Fcs/ACE2-Fc at 1 µg/mL used as detector antibodies (same V_HH-Fc/ACE2-Fc in each column; 20 columns for a total of 19 V_HH-Fcs and ACE2-Fc). The binding of V_HH-Fcs/ACE2-Fc to S1 was detected using 100 µL 1 µg/mL HRP-conjugated goat anti-human IgG (Sigma, Cat#A0170). Finally, plates were washed 10 times with PBST and peroxidase (HRP) activity was determined as described in section "Antigen validation". (d) Bottom-up hydrogen-exchange mass spectrometry. All antibody:antigen complexes were equilibrated at 3:1 ratio in PBS (pH 7.1) at 4 °C prior to labeling. The labeling reaction was initiated upon 10x dilution with 10 mM Tris (45% D_2O) at 20 °C with an HDx3-PAL autosampler (Trajan Scientific and Medical, Ringwood, Australia) for a final composition of 40% D_2O. The reaction was quenched after 3 min by a 5x dilution with 1% formic acid (FA, pH 2.2, 4 °C), and 75 µL (20 pmol) was injected. Labeled sample was flowed through a µ-Prepcell (Antec Scientific, Zoeterwoude, The Netherlands) at 50 µL/min in mobile phase A (0.23% FA) where electrochemical reduction was performed in pulse mode ($E1 = 1.0$ V, $E2 = 0$ V, $t1 = 1$ s, $t2 = 0.1$ s)[95], followed by online digestion with a pepsin (Enzymate BEH, Waters, Milford, MA) or nepenthesin-II column (Affipro, Prague, Czech Republic). Peptides were trapped (Waters ACQUITY UPLC BEH C18 Vanguard Pre-column, 130 Å, 1.7 µm, 2.1 mm × 5 mm), separated (ACQUITY UPLC BEH C18, 130 Å, 1.7 µm, 1 × 100 mm) with an acetonitrile gradient and analyzed by ESI-MS (300–1600 m/z) with a Synapt G2-Si (Waters), with ion mobility enabled for the S dataset. Data-dependent MS/MS acquisition was applied to an unlabeled sample to generate a peptide map, and peptides were identified with a database search in Mascot. Replicate data was collected in triplicate in five separate batches with unique non-binding controls, and deuteration was assigned with HDExaminer v2 (Batch 1–6, Sierra Analytics, Modesto, CA) or MS Studio[96] (Batch 7). Full experimental parameters for each batch are outlined in Supplementary Table 9. Finally, significant changes in deuteration was assigned based on two cutoffs (3× SD and 1-p = 0.98) using MS Studio[97].

Surrogate virus neutralization assays. (a) ACE2 competition assay by ELISA. Wells of NUNC® Immulon 4 HBX microtiter plates (Thermo Fisher) were coated overnight at 4 °C with 50 ng/well of S in 100 µL PBS, pH 7.4. Next day, plates were blocked with 250 µL PBSC for 1 h at room temperature. For ACE2/V_HH competitive binding to SARS-CoV-2 S (Wuhan), 50 µL of human ACE2-Fc (ACROBiosystems, Cat#AC2-H5257) at 400 ng/mL was mixed with 50 µL of V_HH at 1 µM, and then transferred to SARS-CoV-2 S coated microtiter plate wells. After 1 h incubation at room temperature, plates were washed 10 times with PBST and the ACE2-Fc binding was detected using 1 µg/mL goat anti-human IgG (Fc specific) HRP conjugate antibody (Sigma, Cat#A0170) in 100 µL PBSCT. After 10 washes with PBST, the peroxidase (HRP) activity was determined as described in section "Antigen validation". (b) ACE2 competition assay by SPR. Standard SPR techniques were used for binding studies. All SPR assays were performed on a Biacore T200 instrument (Cytiva) at 25 °C with HBS-EP running buffer (10 mM HEPES, 150 mM NaCl, 3 mM EDTA, 0.005% Tween 20, pH 7.4) and CM5 sensor chips (Cytiva). Prior to SPR analyses all analytes in flow (V_HHs, ACE2) were SEC-purified on a Superdex 75™ Increase 10/300 GL column (Cytiva) in HBS-EP buffer at a flow rate of 0.8 mL/min to obtain monomeric proteins. V_HHs were analyzed for their ability to block the SARS-CoV-2 Wuhan S interaction with ACE2 using SPR dual injection experiments. V_HHs and ACE2 were flowed over the SARS-CoV-2 S surface at 40 µL/min in HBS-EP buffer. Dual injections consisted of injection of ACE2 (1 µM) for 150 s, followed by immediate injection of a mixture of ACE2 (1 µM) + V_HH (at 20–40 × K_D concentration) for 150 s. The opposite orientation was also performed (V_HH followed by V_HH + ACE2). Surfaces were regenerated using a 12 s pulse of 10 mM glycine, pH 1.5, at a flow rate of 100 µL/min. All pairwise combinations of V_HHs and ACE2 were analyzed. V_HHs that competed with ACE2 for SARS-CoV-2 spike glycoprotein binding showed no increase in binding response during the second injection. Conversely, a binding response was seen during the second injection for V_HHs that did not compete with ACE2. (c) ACE2 competition assay by flow cytometry. Experiments were performed as described in section "Llama immunization and serum analysis", except that biotinylated S/Vero E6 cells were mixed with V_HHs or V_HH-Fcs instead of sera. In addition, assays were performed against biotinylated SARS-CoV-2 Wuhan, Alpha, Beta, Gamma, Delta, Kappa, and Omicron (B.1.1.529) as well as SARS-CoV S. As internal reference of competition experiments, competition assay with recombinant human ACE2-H_6 in lieu of V_HH was also included. A20.1, a *C. difficile* toxin A-specific V_HH[85] was used as negative control V_HH. Percent inhibition was calculated according the formula in section "Llama immunization and serum analysis", with F_n and F_{max} relating to V_HH not serum as the competitor.

Pseudotyped and live virus neutralization assays. (a) Spike-pseudotyped lentivirus neutralization assays. (i) Generation of SARS-CoV-2 spike pseudotyped lentiviral particles (LVP): HEK293T cells were plated in a 100-mm tissue culture dish and transfected the next day at about 75% confluency with a combination of a lentiviral transfer vector encoding eGFPLuc (addgene#119816), the packaging plasmid psPAX2 (addgene#12260), and a plasmid encoding the viral glycoprotein of interest SARS-CoV-2 Spike-ΔS1/S2-Δ20 expressed in pcDNA3.1$^+$. Transfection was performed using the jetPRIME transfection reagent (Polyplus-transfection,

Illkirch, France) according to the manufacturer's protocol at a 1:1:1 (eGFPLuc:psPAX2:Spike) ratio for a total of 10 µg. The media was replaced at 24 h post transfection and complete media added to the plate. The supernatant from cell culture was harvested at 48, 72, and 96 h, each time replenished with fresh media. The combined supernatants were centrifuged at 800x*g* for 10 min and supernatants passed through a 0.45-µm syringe filter. Then, 1 volume of concentrator (40% [w/v] PEG-8000, 1.2 M NaCl, pH 7.0) was added to 3 volumes of supernatant, mixed for 1 min then incubated with constant rocking at 60 rpm for at least 4 h at 4 °C. The mixture was centrifuged at 1600×*g* for 60 min at 4 °C and the supernatant carefully discarded without disturbing the pellet. The pellet was then resuspended in PBS buffer at 1/10 of the original supernatant volume with gentle up-and-down pipetting, aliquoted and stored at −80 °C. (ii) Viral neutralization assays: HEK293T-hACE2 cell line (BEI Resources, Manassas, VA, Cat#NR-52511) were seeded in poly-L-Lysine (PLL)-coated white, clear bottom 384-wells plate (NUNC, Thermo Fisher) at a density of 9000 cells/well in 45 µL of media (DMEM without phenol red supplemented with 5% [v/v] FBS) and incubated for 24 h at 37 °C, 5% CO_2. The next day, a half-log serial dilution of each nanobody (V_HH/V_HH-Fc) to be tested was prepared at 4× the final concentration ranging from 0 to 50 µg/mL in complete media. Then, 20 µL of the 4× nanobody solution was added to each well and incubated for 10 min at 37 °C, 5% CO_2. After incubation, 20 µL of LVP master mix was added to each well and incubated a further 48 h at 37 °C, 5% CO_2. LVP master mix was prepared as follow: 10 µL of LVPs (as prepared above) were mixed with 20 µg/mL of polybrene (4× final concentration) and media for a final volume of 20 µL per well. Forty-eight hours later, 30 µL of the substrate buffer (324 mM Tris–HCl, 125 mM Tris-Base, 225 mM NaCl, 9 mM $MgCl_2$, 15 mM dithiothreitol (DTT), 0.6 mM coenzyme A, 0.42 mg/mL D-luciferin, 3.3 mM ATP, 0.75% (v/v) Triton X-100, 6 mM sodium hydrosulfite) was added to each well. Then the plate was vortexed at 400 rpm for 2 min and luminescence read on a Synergy Neo2 plate reader (BioTek, Winooski, VT). IC_{50}s were determined from non-linear regression [inhibitor] vs. response, variable slope (four parameters) using GraphPad Prism version 9 (La Jolla, CA). (b) Live virus neutralizations assays. Neutralization activity of antibodies to SARS-CoV-2 was determined with the microneutralization assay. In brief, V_HH-Fc stocks were prepared at 1 mg/mL in PBS and sterilized by passing through 0.22-µm filters. Quantitative microneutralization assay was performed on Vero E6 cells with SARS-CoV-2 strains hCOV-19/Canada/ON-VIDO-01/2020, NR-53565 (Wuhan); hCOV-19/England/204820464/2020, NR-54000 (Alpha); hCOV-19/South Africa/KRISP-EC-K005321 /2020, NR-54008 (Beta); or Isolate hCoV-19/USA/GA-EHC-2811C/2021, NR-56481 (Omicron, Lineage B.1.1.529). In brief, 15 µg of antibody was diluted in 300 µL of infection media (1× DMEM, high glucose media supplemented with 1× nonessential amino acid, 100 U/mL penicillin-streptomycin, 1 mM sodium pyruvate, and 1% FBS), from which a subsequent 1:5 serial dilutions was carried out. Fifty microliters of each antibody dilution was mixed with 250 plaque-forming units (pfu) of virus in 50 µL volume. The virus/antibody mix was incubated at 37 °C for 1 h. Fifty microliters of the virus/antibody mix was used to infect Vero E6 cells for 1 h at 37 °C. The inoculum was removed and 100 µL of antibody dilution was added to each corresponding infected cell monolayer. Infection was incubated at 37 °C for 72 h, from then they were fixed in 10% formaldehyde. Virus infection was detected with mouse mAb to SARS-CoV-2 nucleocapsid (N) (R&D Systems, Minneapolis, MN, Cat#MAB10474) followed by rabbit anti-mouse IgG-HRP (Cedarlane, Cat#610-4302) and developed with *o*-Phenylenediamine dihydrochloride (Sigma) and detected on BioTek Synergy H1 microplate reader at 490 nm. IC_{50}s were determined from non-linear regression [inhibitor] vs. response, variable slope (four parameters) using GraphPad Prism version 9 (La Jolla, CA).

In vivo efficacy studies. (a) In vivo challenge. Six-seven weeks old female LVG Golden Syrian hamsters (90–100 g) were obtained from Charles River Laboratories (Saint-Constant, Canada) and maintained at the NRC small animal facility. All animal procedures and animal husbandry in this study were carried out in accordance to regulations and guidelines outlined under the Canadian Council on Animal Care and approved by the NRC Human Health Therapeutics Animal Care Committee. Sixty hamsters (six/treatment group) were pre-bled for 300 µL of blood followed by IP infusion with 1 mg of antibodies or with PBS 24 h before challenge. Baseline body weights were determined before challenge. The animals were then infected intranasally under ketamine/xylazine with 8.5×10^4 pfu (in 100 µL) of SARS-CoV-2. Daily weight and clinical symptoms were monitored for 5 days post-infection (dpi). At 5 dpi, animals were euthanized and their lungs were collected for virus titers determination and immunohistochemistry studies. Virus titer was determined by plaque assay on Vero cells. (b) Immunohistochemistry. Lungs were immersed in 10% neutral buffered formalin and fixed for 1 week at room temperature and then transferred into 70% ethanol. All 4 lobes of right lung were processed and embedded in paraffin wax. The paraffin block was cut into 5-µm sections and placed on Superfrost Plus slides (Thermo Fisher). Sections were dried overnight and then subjected to immunohistochemistry (IHC) using a modified protocol F on the Bond-Max III fully automated staining system (Leica Biosystems, Wetzlar, Germany). All reagents from the Bond Polymer Refine Detection Kit DC9800 (Leica, Buffalo Grove, IL) containing peroxide block, post primary, polymer reagent, 3, 3′-diaminobenzidine (DAB) chromogen and hematoxylin counterstain were used for IHC. Following deparaffinization and rehydration, sections were pre-treated with the Epitope Retrieval Solution 1 (ER1, Citrate buffer, pH 5.0) or Epitope Retrieval Solution 2 (ER2, EDTA buffer, pH 8.8) at 98 °C for 20 min. ER1 was used for Iba-1 and SARS-CoV-2 Nucleocapsid and ER2 for CD3. Monoclonal mouse anti-SARS-CoV-2 Nucleocapsid l antibody (1:5000, R&D Systems, Cat#MAB10474) was used for the detection of SARS-CoV-2. Immune cell infiltrate was detected using rabbit polyclonal antibodies against CD3 (1:500, Dako, Cat#A0452), and Iba-1 (ionized calcium binding adapter protein, 1:2000, Wako, Cat#019-19741). Positive signals were detected as brown precipitate at the site of antigen-antibody reaction and nuclei were counterstained blue with hematoxylin. Sections were then dehydrated, cleared and mounted using the Leica fully automated glass coverslipper (CV5030, Leica Biosystems, Wetzlar, Germany). Each antibody was titrated and optimized for the detection of positive signals. Negative controls included omission of primary antibody and incubation with secondary antibody alone as well as lung tissue from naïve animals.

The DeadEnd Colorimetric TUNEL (TdT-mediated dUTP Nick-End Labeling) System (Promega Madison, WI, Cat#G7132) was used to detect apoptosis as per manufacturer's instructions. Briefly, sections were deparaffinized and permeabilized with proteinase K for 15 min followed by labeling with biotinylated nucleotides in the presence of recombinant terminal deoxynucleotidyl transferase. Sections were then incubated with horseradish peroxidase-streptavidin conjugate and developed using DAB for 10 min. Sections were washed and counterstained for 5 min with hematoxylin, dehydrated, cleared and mounted. All images were acquired with an Olympus IX81 microscope, equipped with a DP27 color CCD camera using the ×20 objective (Shinjuku, Tokyo, Japan).

Statistics and reproducibility. Data generated in technical or biological replicates were analyzed in GraphPad Prism v9 and shown in graphs as mean ± SD or SEM. ELISA data on assessing the effect of aerosolization on the functionality of V_HHs were generated in technical duplicates. EC_{50}s were determined by fitting the binding data to non-linear regression [inhibitor] vs. response, variable slope (four parameters) model. Serum SVNAs, PVNAs and LVNAs data were obtained from two, three and two technical replicates, respectively, and IC_{50}s were determined by fitting the inhibition data to the aforementioned model. For in vivo efficacy studies, power calculation was used to determine minimal sample size per group that will give a Power of 80% for a *p*-value of 0.05. The sample size was determined to be a minimum of six hamsters per group. In vivo efficacy data generated from five (VHH-72, S2A3) or six (PBS, isotype, 1d, 05, MRed05, SR01, 1d/MRed05, 1d/SR01) biological replicates (animals) were subjected to statistical analysis as described in Fig. 6 legend. A $p > 0.05$ was considered as not significant. The exact *p*-values are included in Supplementary Data 1.

Reporting summary. Further information on research design is available in the Nature Research Reporting Summary linked to this article.

Data availability

The data generated and/or analyzed during the current study are available from the corresponding author upon request. The source data for figures and tables are provided in Supplementary Information and Supplementary Data 1.

Received: 7 January 2022; Accepted: 22 August 2022;
Published online: 09 September 2022

References

1. Krause, P. R. et al. SARS-CoV-2 variants and vaccines. *N. Engl. J. Med* **385**, 179–186 (2021).
2. Chaqroun A., Hartard C., Schvoerer E. Anti-SARS-CoV-2 vaccines and monoclonal antibodies facing viral variants. *Viruses* **13**, 1171 (2021).
3. Planas, D. et al. Reduced sensitivity of SARS-CoV-2 variant Delta to antibody neutralization. *Nature* **596**, 276–280 (2021).
4. Li, T. et al. A synthetic nanobody targeting RBD protects hamsters from SARS-CoV-2 infection. *Nat. Commun.* **12**, 4635 (2021).
5. Madhi, S. A. et al. Efficacy of the ChAdOx1 nCoV-19 Covid-19 vaccine against the B.1.351 variant. *N. Engl. J. Med.* **384**, 1885–1898 (2021).
6. Chen, R. E. et al. Resistance of SARS-CoV-2 variants to neutralization by monoclonal and serum-derived polyclonal antibodies. *Nat. Med.* **27**, 717–726 (2021).
7. Li, Y. et al. Linear epitope landscape of the SARS-CoV-2 Spike protein constructed from 1,051 COVID-19 patients. *Cell Rep.* **34**, 108915 (2021).
8. Kaku, Y. et al. Resistance of SARS-CoV-2 variants to neutralization by antibodies induced in convalescent patients with COVID-19. *Cell Rep.* **36**, 109385 (2021).
9. Cameroni, E. et al. Broadly neutralizing antibodies overcome SARS-CoV-2 Omicron antigenic shift. *Nature* **602**, 664–670 (2022).
10. Ke, Z. et al. Structures and distributions of SARS-CoV-2 spike proteins on intact virions. *Nature* **588**, 498–502 (2020).

11. Lan, J. et al. Structure of the SARS-CoV-2 spike receptor-binding domain bound to the ACE2 receptor. *Nature* **581**, 215–220 (2020).
12. Yan, R. et al. Structural basis for the recognition of SARS-CoV-2 by full-length human ACE2. *Science* **367**, 1444–1448 (2020).
13. Wrapp, D. et al. Cryo-EM structure of the 2019-nCoV spike in the prefusion conformation. *Science* **367**, 1260–1263 (2020).
14. Walls, A. C. et al. Structure, function, and antigenicity of the SARS-CoV-2 spike glycoprotein. *Cell* **181**, 281–292.e286 (2020).
15. Cerutti, G. et al. Potent SARS-CoV-2 neutralizing antibodies directed against spike N-terminal domain target a single supersite. *Cell Host Microbe* **29**, 819–833 e817 (2021).
16. Cerutti, G. et al. Neutralizing antibody 5-7 defines a distinct site of vulnerability in SARS-CoV-2 spike N-terminal domain. *Cell Rep.* **37**, 109928 (2021).
17. McCallum, M. et al. N-terminal domain antigenic mapping reveals a site of vulnerability for SARS-CoV-2. *Cell* **184**, 2332–2347.e2316 (2021).
18. Suryadevara, N. et al. Neutralizing and protective human monoclonal antibodies recognizing the N-terminal domain of the SARS-CoV-2 spike protein. *Cell* **184**, 2316–2331.e2315 (2021).
19. Greaney, A. J. et al. Mapping mutations to the SARS-CoV-2 RBD that escape binding by different classes of antibodies. *Nat. Commun.* **12**, 4196 (2021).
20. Chi, X. et al. A neutralizing human antibody binds to the N-terminal domain of the Spike protein of SARS-CoV-2. *Science* **369**, 650–655 (2020).
21. Zheng Z., et al. Monoclonal antibodies for the S2 subunit of spike of SARS-CoV-1 cross-react with the newly-emerged SARS-CoV-2. *Euro Surveill.* **25**, 2000291 (2020).
22. Fan, X., Cao, D., Kong, L. & Zhang, X. Cryo-EM analysis of the post-fusion structure of the SARS-CoV spike glycoprotein. *Nat. Commun.* **11**, 3618 (2020).
23. Esparza, T. J., Martin, N. P., Anderson, G. P., Goldman, E. R. & Brody, D. L. High affinity nanobodies block SARS-CoV-2 spike receptor binding domain interaction with human angiotensin converting enzyme. *Sci. Rep.* **10**, 22370 (2020).
24. Xiang, Y. et al. Versatile and multivalent nanobodies efficiently neutralize SARS-CoV-2. *Science* **370**, 1479–1484 (2020).
25. Schoof, M. et al. An ultrapotent synthetic nanobody neutralizes SARS-CoV-2 by stabilizing inactive Spike. *Science* **370**, 1473–1479 (2020).
26. Custodio, T. F. et al. Selection, biophysical and structural analysis of synthetic nanobodies that effectively neutralize SARS-CoV-2. *Nat. Commun.* **11**, 5588 (2020).
27. Hanke, L. et al. An alpaca nanobody neutralizes SARS-CoV-2 by blocking receptor interaction. *Nat. Commun.* **11**, 4420 (2020).
28. Dong, J. et al. Development of humanized tri-specific nanobodies with potent neutralization for SARS-CoV-2. *Sci. Rep.* **10**, 17806 (2020).
29. Huo, J. et al. Neutralizing nanobodies bind SARS-CoV-2 spike RBD and block interaction with ACE2. *Nat. Struct. Mol. Biol.* **27**, 846–854 (2020).
30. Wrapp, D. et al. Structural basis for potent neutralization of betacoronaviruses by single-domain camelid antibodies. *Cell* **181**, 1004–1015 e1015 (2020).
31. Chi, X. et al. Humanized single domain antibodies neutralize SARS-CoV-2 by targeting the spike receptor binding domain. *Nat. Commun.* **11**, 4528 (2020).
32. Koenig, P. A., et al. Structure-guided multivalent nanobodies block SARS-CoV-2 infection and suppress mutational escape. *Science* **371**, eabe6230 (2021).
33. Li, W. et al. High potency of a bivalent human V_H domain in SARS-CoV-2 animal models. *Cell* **183**, 429–441 e416 (2020).
34. Pymm, P. et al. Nanobody cocktails potently neutralize SARS-CoV-2 D614G N501Y variant and protect mice. *Proc Natl Acad Sci USA* **118**, e2101918118 (2021).
35. Xu, J. et al. Nanobodies from camelid mice and llamas neutralize SARS-CoV-2 variants. *Nature* **595**, 278–282 (2021).
36. Lu, Q. et al. Development of multivalent nanobodies blocking SARS-CoV-2 infection by targeting RBD of spike protein. *J. Nanobiotechnol.* **19**, 33 (2021).
37. Rujas, E. et al. Multivalency transforms SARS-CoV-2 antibodies into ultrapotent neutralizers. *Nat. Commun.* **12**, 3661 (2021).
38. Yao, H. et al. A high-affinity RBD-targeting nanobody improves fusion partner's potency against SARS-CoV-2. *PLoS Pathog.* **17**, e1009328 (2021).
39. Schepens, B. et al. An affinity-enhanced, broadly neutralizing heavy chain-only antibody protects against SARS-CoV-2 infection in animal models. *Sci. Transl. Med.* **13**, eabi7826 (2021).
40. Wu, X. et al. A potent bispecific nanobody protects hACE2 mice against SARS-CoV-2 infection via intranasal administration. *Cell Rep.* **37**, 109869 (2021).
41. Nambulli, S. et al. Inhalable Nanobody (PiN-21) prevents and treats SARS-CoV-2 infections in Syrian hamsters at ultra-low doses. *Science advances* **7**, eabh0319 (2021).
42. Bracken, C. J. et al. Bi-paratopic and multivalent VH domains block ACE2 binding and neutralize SARS-CoV-2. *Nat. Chem. Biol.* **17**, 113–121 (2021).
43. Zupancic, J. M. et al. Engineered multivalent nanobodies potently and broadly neutralize SARS-CoV-2 variants. *Adv. Ther. (Weinh.)* **4**, 2100099 (2021).
44. Chen, X., Gentili, M., Hacohen, N. & Regev, A. A cell-free nanobody engineering platform rapidly generates SARS-CoV-2 neutralizing nanobodies. *Nat. Commun.* **12**, 5506 (2021).
45. Sun, D. et al. Potent neutralizing nanobodies resist convergent circulating variants of SARS-CoV-2 by targeting diverse and conserved epitopes. *Nat. Commun.* **12**, 4676 (2021).
46. Ye, G. et al. The development of Nanosota-1 as anti-SARS-CoV-2 nanobody drug candidates. *Elife* **10**, e64815 (2021).
47. Huo, J. et al. A potent SARS-CoV-2 neutralising nanobody shows therapeutic efficacy in the Syrian golden hamster model of COVID-19. *Nat. Commun.* **12**, 5469 (2021).
48. Hamers-Casterman, C. et al. Naturally occurring antibodies devoid of light chains. *Nature* **363**, 446–448 (1993).
49. NIH. Dose-finding, safety, and efficacy study of XVR011 added to standard of care in patients Hospitalised for COVID-19. https://ClinicalTrials.gov/show/NCT04884295.
50. Detalle, L. et al. Generation and characterization of ALX-0171, a potent novel therapeutic nanobody for the treatment of respiratory syncytial virus infection. *Antimicrob. Agents Chemother.* **60**, 6–13 (2016).
51. Martinez-Delgado, G. Inhaled nanobodies against COVID-19. *Nat. Rev. Immunol.* **20**, 593 (2020).
52. Gai, J. et al. A potent neutralizing nanobody against SARS-CoV-2 with inhaled delivery potential. *MedComm* **2**, 101–113 (2021).
53. Wu, K., Li, W., Peng, G. & Li, F. Crystal structure of NL63 respiratory coronavirus receptor-binding domain complexed with its human receptor. *Proc. Natl Acad. Sci. USA* **106**, 19970–19974 (2009).
54. van der Hoek, L., Pyrc, K. & Berkhout, B. Human coronavirus NL63, a new respiratory virus. *FEMS Microbiol. Rev.* **30**, 760–773 (2006).
55. Dumoulin, M. et al. Single-domain antibody fragments with high conformational stability. *Protein Sci.* **11**, 500–515 (2002).
56. Myers, J. K., Pace, C. N. & Scholtz, J. M. Denaturant m values and heat capacity changes: relation to changes in accessible surface areas of protein unfolding. *Protein Sci.* **4**, 2138–2148 (1995).
57. Vincke, C. et al. General strategy to humanize a camelid single-domain antibody and identification of a universal humanized nanobody scaffold. *J. Biol. Chem.* **284**, 3273–3284 (2009).
58. Ewert, S., Cambillau, C., Conrath, K. & Plückthun, A. Biophysical properties of camelid V_{HH} domains compared to those of human V_H3 domains. *Biochemistry* **41**, 3628–3636 (2002).
59. Govaert, J. et al. Dual beneficial effect of interloop disulfide bond for single domain antibody fragments. *J. Biol. Chem.* **287**, 1970–1979 (2012).
60. Narang, D., James, D. A., Balmer, M. T. & Wilson, D. J. Protein footprinting, conformational dynamics, and core interface-adjacent neutralization "hotspots" in the SARS-CoV-2 spike protein receptor binding domain/human ACE2 interaction. *J. Am. Soc. Mass Spectrom.* **32**, 1593–1600 (2021).
61. Hansen, J. et al. Studies in humanized mice and convalescent humans yield a SARS-CoV-2 antibody cocktail. *Science* **369**, 1010–1014 (2020).
62. Dumet, C. J. Y. et al. Exploring epitope and functional diversity of anti-SARS-CoV2 antibodies using AI-based methods. *BioRxiv* https://doi.org/10.1101/2020.12.23.424199 (2020).
63. Henderson, R. et al. Controlling the SARS-CoV-2 spike glycoprotein conformation. *Nat. Struct. Mol. Biol.* **27**, 925–933 (2020).
64. Wang, N. et al. Structure-based development of human antibody cocktails against SARS-CoV-2. *Cell Res.* **31**, 101–103 (2021).
65. Voss, W. N. et al. Prevalent, protective, and convergent IgG recognition of SARS-CoV-2 non-RBD spike epitopes. *Science* **372**, 1108–1112 (2021).
66. Li, D. et al. The functions of SARS-CoV-2 neutralizing and infection-enhancing antibodies in vitro and in mice and nonhuman primates. *BioRxiv* https://doi.org/10.1101/2020.12.31.424729 (2021).
67. Wang, P. et al. Increased resistance of SARS-CoV-2 variant P.1 to antibody neutralization. *Cell Host Microbe* **29**, 747–751 e744 (2021).
68. Richard, G. et al. In vivo neutralization of α-cobratoxin with high-affinity llama single-domain antibodies (V_HHs) and a V_HH-Fc antibody. *PLoS ONE* **8**, e69495 (2013).
69. Godakova, S. A., et al. Camelid VHHs fused to human Fc fragments provide long term protection against botulinum neurotoxin A in mice. *Toxins* **11**, 464 (2019).
70. Tostanoski, L. H. et al. Ad26 vaccine protects against SARS-CoV-2 severe clinical disease in hamsters. *Nat. Med.* **26**, 1694–1700 (2020).
71. Barnes, C. O. et al. SARS-CoV-2 neutralizing antibody structures inform therapeutic strategies. *Nature* **588**, 682–687 (2020).
72. Barnes, C. O. et al. Structures of human antibodies bound to SARS-CoV-2 spike reveal common epitopes and recurrent features of antibodies. *Cell* **182**, 828–842.e816 (2020).
73. Yuan, M. et al. Structural basis of a shared antibody response to SARS-CoV-2. *Science* **369**, 1119–1123 (2020).

74. Huang, Y. N. A. et al. Identification of a conserved neutralizing epitope present on spike proteins from all highly pathogenic coronaviruses. *BioRxiv* https://doi.org/10.1101/2021.01.31.428824 (2021).
75. Lu, Y. W. J., Li, Q., Hu, H., Lu, J. & Chen, Z. Advances in neutralization assays for SARS-CoV-2. *Scand. J. Immunol.* **e13088**, 1–15 (2021). *2021 Jun 16.*
76. Beaudoin-Bussieres, G. et al. A Fc-enhanced NTD-binding non-neutralizing antibody delays virus spread and synergizes with a nAb to protect mice from lethal SARS-CoV-2 infection. *Cell Rep.* **38**, 110368 (2022).
77. Ullah, I. et al. Live imaging of SARS-CoV-2 infection in mice reveals that neutralizing antibodies require Fc function for optimal efficacy. *Immunity* **54**, 2143–2158 e2115 (2021).
78. Schepens, B. et al. Nanobodies® specific for respiratory syncytial virus fusion protein protect against infection by inhibition of fusion. *J. Infect. Dis.* **204**, 1692–1701 (2011).
79. Stuible, M. et al. Rapid, high-yield production of full-length SARS-CoV-2 spike ectodomain by transient gene expression in CHO cells. *J. Biotechnol.* **326**, 21–27 (2021).
80. Sulea, T. et al. Structure-based dual affinity optimization of a SARS-CoV-1/2 cross-reactive single-domain antibody. *PLoS ONE* **17**, e0266250 (2022).
81. Akache, B. et al. Immunogenic and efficacious SARS-CoV-2 vaccine based on resistin-trimerized spike antigen SmT1 and SLA archaeosome adjuvant. *Sci. Rep.* **11**, 21849 (2021).
82. Galipeau, Y. et al. Relative ratios of human seasonal coronavirus antibodies predict the efficiency of cross-neutralization of SARS-CoV-2 spike binding to ACE2. *EBioMedicine* **74**, 103700 (2021).
83. Colwill, K. et al. A scalable serology solution for profiling humoral immune responses to SARS-CoV-2 infection and vaccination. *Clin. Transl. Immunol.* **11**, e1380 (2022).
84. Rossotti, M. et al. Streamlined method for parallel identification of single domain antibodies to membrane receptors on whole cells. *Biochim Biophys. Acta* **1850**, 1397–1404 (2015).
85. Hussack, G. et al. Neutralization of *Clostridium difficile* toxin A with single-domain antibodies targeting the cell receptor binding domain. *J. Biol. Chem.* **286**, 8961–8976 (2011).
86. Henry, K. A. et al. Isolation of TGF-β-neutralizing single-domain antibodies of predetermined epitope specificity using next-generation DNA sequencing. *Protein Eng. Des. Sel.* **29**, 439–443 (2016).
87. Rossotti, M. A. et al. Camelid single-domain antibodies raised by DNA immunization are potent inhibitors of EGFR signaling. *Biochem J.* **476**, 39–50 (2019).
88. Rossotti, M. A. et al. Method for sorting and pairwise selection of nanobodies for the development of highly sensitive sandwich immunoassays. *Anal. Chem.* **87**, 11907–11914 (2015).
89. Poulain, A. et al. Rapid protein production from stable CHO cell pools using plasmid vector and the cumate gene-switch. *J. Biotechnol.* **255**, 16–27 (2017).
90. Henry, K. A. et al. Stability-diversity tradeoffs impose fundamental constraints on selection of synthetic human V_H/V_L single-domain antibodies from In vitro display libraries. *Front. Immunol.* **8**, 1759 (2017).
91. Wafer, L., Kloczewiak, M., Polleck, S. M. & Luo, Y. Isothermal chemical denaturation of large proteins: Path-dependence and irreversibility. *Anal. Biochem.* **539**, 60–69 (2017).
92. Saerens, D., Conrath, K., Govaert, J. & Muyldermans, S. Disulfide bond introduction for general stabilization of immunoglobulin heavy-chain variable domains. *J. Mol. Biol.* **377**, 478–488 (2008).
93. Delfin-Riela, T., Rossotti, M. A., Echaides, C. & Gonzalez-Sapienza, G. A nanobody-based test for highly sensitive detection of hemoglobin in fecal samples. *Anal. Bioanal. Chem.* **412**, 389–396 (2020).
94. Delfin-Riela T., Rossotti M., Alvez-Rosado R., Leizagoyen C., Gonzalez-Sapienza G. Highly sensitive detection of Zika virus nonstructural protein 1 in serum samples by a two-site nanobody ELISA. *Biomolecules* **10**, 1652 (2020).
95. Comamala, G. et al. Hydrogen/deuterium exchange mass spectrometry with improved electrochemical reduction enables comprehensive epitope mapping of a therapeutic antibody to the cysteine-knot containing vascular endothelial growth factor. *Anal. Chim. Acta* **1115**, 41–51 (2020).
96. Rey, M. et al. Mass spec studio for integrative structural biology. *Structure* **22**, 1538–1548 (2014).
97. Raval, S. et al. Improving spectral validation rates in hydrogen-deuterium exchange data analysis. *Anal. Chem.* **93**, 4246–4254 (2021).
98. Tamura, K., Stecher, G. & Kumar, S. MEGA11: molecular evolutionary genetics analysis version 11. *Mol. Biol. Evol.* **38**, 3022–3027 (2021).

Acknowledgements

We thank Bassam Hallis for contributing SARS-Related Coronavirus 2, Isolate hCoV-19/England/204820464/2020, NR-54000 (Alpha variant), Alex Sigal and Tulio de Oliveira for contributing SARS-Related Coronavirus 2, Isolate hCoV-19/South Africa/KRISP-EC-K005321/2020, NR-54008 (Beta variant), and Mehul Suthar for contributing SARS-Related Coronavirus 2, Isolate hCoV-19/USA/GA-EHC-2811C/2021 (Lineage B.1.1.529; Omicron variant), NR-56481; all virus isolates were obtained through BEI Resources, NIAID, NIH. We thank the NRC Animal Resources team for animal husbandry and technical support, and Luc Lemay and Jennifer Wellman for technical support in the CL3. We thank Sonia Leclerc and Julie Haukenfrers for performing DNA sequencing. We thank Qingling Yang and Shannon Ryan for assistance with expression of ACE2-H_6 and His tagged and Fc-fused RBD/SD1, and Mary Foss for assistance with aerosolization studies. We thank the NRC Mammalian Cell Expression Section for assistance with production of recombinant proteins and Joline Cormier for contribution to protein samples management. We thank Alina Burlacu for generating the CHO-SPK cells and Tahir Maqbool for his support with llama immunizations, blood collection and cell preparation. We thank Unchained Labs (Pleasanton, CA) for conducting isothermal chemical denaturation experiments. This work was supported by funding from the Pandemic Response Challenge Program of the National Research Council Canada and in part by a CIHR grant (OV1 - 170355) to M.-A.L.

Author contributions

M.A.R. and J.T. conceived the experiments, designed assays, and analyzed all data. M.A.R. performed library construction, selection campaigns and screening experiments, ELISA binding and specificity assays, cell binding experiments by flow cytometry, ELISA- and flow cytometry-based SVNAs, and epitope typing experiments. M.A.R. and X.W. expressed and purified V_HHs and V_HH-Fcs at various scales for characterization and animal studies, and performed SEC and stability studies. Y.D., C.G., M.S., J.G., and S.P. designed, expressed, and purified spike glycoprotein fragments and assisted with the production of V_HH-Fcs. H.vF. and G.H. designed, performed and analyzed SPR binding affinity/specificity, epitope binning and ACE2 competition experiments. M.-A.L. designed pseudotyped virus neutralization assays and analyzed the data. K.M., G.L., and P.M.G. performed the pseudotyped virus neutralization assays and collected the data. A.T. designed, performed and analyzed in vivo animal study and live virus neutralization assays. D.D. performed in vivo animal challenge, necropsy and plaque assay. S.B. performed in vivo animal challenge and necropsy. J.B. performed in vivo animal challenge, necropsy and plaque assay. J.K.S. conceptualized the immunohistochemical studies and analyzed the data. M.H. performed the immunohistochemical experiments and collected the data. J.S. designed, performed and analyzed HDX/MS experiments. J.T. acquired and dispersed the project fund and supervised the overall study. J.T. and M.A.R. wrote the manuscript with input from G.H., J.K.S., J.S., and A.T. All authors read, provided input on and approved of the final manuscript.

Competing interests

The authors M.A.R. and J.T. declare the following competing interests: National Research Council Canada has filed a patent (PCT/IB2022/053756, "Antibodies that bind SARS-CoV-2 spike protein") that includes the 37 V_HHs described here, M.A.R. and J.T. are named as inventors. All other authors declare no competing interests.

Additional information

Supplementary information The online version contains supplementary material available at https://doi.org/10.1038/s42003-022-03866-z.

Correspondence and requests for materials should be addressed to Jamshid Tanha.

Peer review information *Communications Biology* thanks Xiangxi Wang and the other, anonymous, reviewer(s) for their contribution to the peer review of this work. Primary Handling Editors: Anam Akhtar and Gene Chong.

Reprints and permission information is available at http://www.nature.com/reprints

Publisher's note Springer Nature remains neutral with regard to jurisdictional claims in published maps and institutional affiliations.

Open Access This article is licensed under a Creative Commons Attribution 4.0 International License, which permits use, sharing, adaptation, distribution and reproduction in any medium or format, as long as you give appropriate credit to the original author(s) and the source, provide a link to the Creative Commons license, and indicate if changes were made. The images or other third party material in this article are included in the article's Creative Commons license, unless indicated otherwise in a credit line to the material. If material is not included in the article's Creative Commons license and your intended use is not permitted by statutory regulation or exceeds the permitted use, you will need to obtain permission directly from the copyright holder. To view a copy of this license, visit http://creativecommons.org/licenses/by/4.0/.

© Crown 2022